Geochimica et Cosmochimica Acta 417 (2026) 135–149

Contents lists available at ScienceDirect

Geochimica et Cosmochimica Acta

journal homepage: www.elsevier.com/locate/gca

Antimony coprecipitation suppresses microbial reduction of goethite and hematite and limits Sb release across particle sizes

Xiyang Xu [a], Prachi Joshi [a,b], Kerstin Hockmann [c], Carolin L. Dreher [a], Valerie A. Schoepfer [d], Po-Yen Tung [e,f], John C. Walmsley [e], Andreas Kappler [a], Muammar Mansor [a,*]

[a] Geomicrobiology, Department of Geosciences, University of Tübingen 72076 Tübingen Germany
[b] Forest Soils and Biogeochemistry, Swiss Federal Institute for Forest Snow and Landscape Research, CH-8903 Birmensdorf, Switzerland
[c] Applied Geochemistry, Institute of Earth and Environmental Sciences, University of Freiburg 79104 Freiburg, Germany
[d] Environmental Geochemistry, Department of Geological Sciences, University of Saskatchewan, S7N 5E2 Saskatoon, Canada
[e] Electron Microscopy Group, Department of Materials Science and Metallurgy, University of Cambridge CB3 0FS Cambridge, UK
[f] Department of Earth Sciences, University of Cambridge CB2 3EQ Cambridge, UK

ARTICLE INFO

Associate editor: Caroline L. Peacock

Keywords:
Goethite
Hematite
Nanoparticles
Antimony
microbial Fe(III) reduction

ABSTRACT

Antimony (Sb) is a toxic environmental contaminant, whose environmental behaviour is tightly linked to sorption or co-precipitation reactions with iron(III) (oxyhydr)oxides. These nanoparticulate minerals are susceptible to reductive dissolution via the activity of dissimilatory Fe(III)-reducing microorganisms (DIRB), thereby potentially mobilizing associated Sb. However, the impacts of Sb (generally in the form of Sb(V)) associated with iron(III) (oxyhydr)oxides of different particle sizes on microbial Fe(III) reduction, as well as on subsequent Sb speciation and distribution, remain poorly understood. In this study, we synthesized Sb(V)-containing goethite and hematite of varying particle sizes and characterized them using micro X-ray diffraction (μ-XRD), scanning/transmission electron microscopy (S/TEM), ^{57}Fe Mössbauer spectroscopy, extended X-ray absorption fine structure (EXAFS) spectroscopy, and wet chemical extractions. We then examined their reductive dissolution by *Shewanella oneidensis* MR-1. Our findings reveal that (i) Sb(V) was incorporated into nanoscale iron(III) (oxyhydr)oxides to varying extents (Sb: Fe ratios ranging from 2:100 to 8:100), with no clear correlation between the extent of coprecipitation and mineral type or particle size. (ii) The presence of Sb(V) significantly inhibited both the extent and kinetics of microbial Fe(III) reduction across all samples of varying particle sizes, with suppression extent ranging from 25 to 80%. (iii) Sb release was limited (<10% of total Sb for goethite and <4% of total Sb for hematite), exhibited incongruence with the reductive dissolution of Fe, and showed only negligible Sb(V) reduction to Sb(III) across all sample conditions. These collective results indicate that the incorporation of Sb(V) into goethite and hematite may enhance the stability of these iron(III) (oxyhydr)oxides and serve as an effective sink for Sb immobilization. This stabilization persists even under reducing conditions, highlighting the potential for long-term Sb sequestration in Fe-rich environments.

1. Introduction

Antimony (Sb) has been declared as a priority environmental pollutant, with chronic exposure associated with cancer and lung, heart, and gastrointestinal diseases (Cooper and Harrison, 2009; Herath et al., 2017). Despite its hazardous nature, Sb is used in numerous products in our daily life, including plastic, batteries, and glassware (Filella et al., 2020). Due to the rapid growth in its industrial use, the global production of Sb is expected to remain high until 2050 (Zhou et al., 2015). This results in a steadily growing legacy of environmental Sb contamination, which is often exacerbated by unmonitored release of Sb into aquatic ecosystems (Filella et al., 2002a; Filella et al., 2009; Fu et al., 2023).

In natural aquatic environments, Sb occurs mainly in the +III and +V redox states. Under oxic to slightly reducing conditions, Sb(V), mainly as $Sb(OH)_6^-$, is the dominant Sb species, while Sb(III) is more stable under

* Corresponding author.
E-mail address: muammar.mansor@uni-tuebingen.de (M. Mansor).

https://doi.org/10.1016/j.gca.2026.01.034
Received 14 July 2025; Accepted 22 January 2026
Available online 29 January 2026

strongly reducing conditions (Filella et al., 2002b; Wilson et al., 2010; He et al., 2019). The environmental behaviour of both Sb species has been shown to be tightly linked to sorption or co-precipitation reactions with iron(III) minerals (Yan et al., 2022a; Wang et al., 2024; Jang et al., 2025). Among these minerals, goethite and hematite (hereafter referred to as iron(III) (oxyhydr)oxides) are two of the most abundant and geochemically significant iron(III) minerals present in soils and sediments (Journet et al., 2014), and are frequently found in Sb-impacted regions, such as the Ichinokawa Sb mine (Japan), Beaver Brook Sb deposit (Canada), and Xikuangshan mining area (China), where they play a major role in controlling the long-term sequestration and mobility of Sb (Mitsunobu et al., 2010; Radková et al., 2020; Zhou et al., 2024). For example, Sb(V) cannot only undergo surface sorption with goethite and hematite in both laboratory and natural samples (Guo et al., 2014; Qiu et al., 2018), but can also be structurally incorporated into those thermodynamically stable solid phases (Mitsunobu et al., 2010; Mitsunobu et al., 2013).

Despite the clear environmental relevance of such processes, the early-stage behavior of Sb(V)- coprecipitated iron(III) (oxyhydr)oxides under different redox conditions remains poorly understood. Only a few studies have investigated the behavior of Sb in Sb-bearing ferrihydrite, a poorly crystalline and metastable iron(III) mineral, under reducing conditions using dissimilatory Fe(III)-reducing bacteria and abiotic aqueous Fe(II) (Burton et al., 2019; Zegeye et al., 2021; Xie et al., 2023; Jang et al., 2025). Sb-coprecipitated goethite is sometimes formed as a secondary mineral product in these studies. However, no study to date has systematically investigated the reduction behavior of Sb-bearing goethite and hematite (which are commonly closely associated with Sb species), nor characterized the Sb mobility and resulting secondary minerals under microbial reducing conditions. Furthermore, depending on the environmental conditions, the formed iron(III) (oxyhydr)oxides may vary in size from nanometer to micrometer scale (Hochella Jr. et al., 2008). Nanoparticles behave remarkably differently from their larger counterparts, resulting in enhanced roles in the biogeochemical cycling and fate of trace elements and contaminants via redox reactions (Borch et al., 2010; Mansor and Xu, 2020; Kappler et al., 2021). For example, iron(III) (oxyhydr)oxide minerals are susceptible to microbial Fe(III) reduction under anoxic conditions, with the extent and rate of reduction increasing with smaller particle size, but not predictable from particle mineral characterization alone (Yan et al., 2008; Echigo et al., 2012; Liu et al., 2016; Xu et al., 2025). Therefore, accurately determining the effects of particle size on reduction behaviour of Sb-containing goethite and hematite require further systematic investigation.

While reductive dissolution of iron(III) (oxyhydr)oxides may release associated Sb into solution, the higher sorption capacities of smaller particles may compensate for this effect via re-adsorption of the released Sb (Borch et al., 2010; Xu et al., 2025). In addition, Sb may itself participate in electron transfer reactions: Sb(V) may undergo reduction to Sb(III) under reducing conditions, either abiotically by Fe(II)-bearing minerals or via microbial activity (Kirsch et al., 2008; Mitsunobu et al., 2008; Zhang et al., 2022). This is particularly significant because Sb(III) adsorbs more strongly to iron(III) (oxyhydr)oxides and is more toxic to ecosystems than Sb(V) (Filella et al., 2002a). Collectively, the net effect of these complex reaction networks on the fate of Sb remains uncertain.

In this study, we systematically investigated the reduction behavior of Sb-containing iron(III) (oxyhydr)oxides as a function of particle size using a microbially mediated reduction approach. The work had three specific objectives: (i) To assess the coprecipitation behavior and partitioning of Sb in goethite and hematite across varying particle sizes. (ii) To evaluate the impact of coprecipitated Sb on the reduction kinetics and extent of Sb-containing goethite and hematite as a function of particle size. (iii) To evaluate the speciation and distribution of coprecipitated Sb following microbial reduction across samples with varying particle sizes. To achieve these objectives, we synthesized the iron(III) (oxyhydr)oxides, goethite and hematite, with different particle sizes in the presence of Sb, resulting in Sb-Fe-coprecipitates with varying concentrations. Then we incubated Sb-containing goethite and hematite of varying particle sizes with the Fe(III)-reducing bacterium *Shewanella oneidensis* MR-1. We characterized the samples before and after reduction using micro X-ray diffractometry (μ-XRD), scanning/transmission electron microscopy (S/TEM), ^{57}Fe Mössbauer spectroscopy, and extended X-ray absorption fine structure (EXAFS) spectroscopy, and tracked the reduction of Fe(III) using wet chemical extraction techniques. The findings of this research enhance our understanding of the reduction susceptibility of Sb-containing iron(III) (oxyhydr)oxides and the associated geochemical mobility of Sb with varying particle sizes in natural environments.

2. Materials and methods

2.1. Synthesis of Sb(V)- coprecipitated and Sb(V)- free iron(III) (oxyhydr)oxides

Goethite (Gt) and hematite (Hm) with varying particle sizes were synthesized based on our previous methods (Xu et al., 2025). The synthesized minerals are referred to as Large Gt, Medium Gt, Small Gt, and Large Hm, Medium Hm, Small Hm based on their respective particle size. Details regarding the synthesis procedures are provided in the SI, Section S1.

Antimony(V)- coprecipitated goethite and hematite were prepared via a slight modification of the methods described in the SI (Section S1.1). A solution of $KSb(OH)_6$ was initially added to the synthesis solution to achieve an Fe(III)/Sb(V) molar ratio of 10:1. This level of Sb(V) loading was selected to be representative of the high levels of Sb(V)-accumulated particles at natural Sb-contaminated sites (Mitsunobu et al., 2010). Sb(V), weakly adsorbed on the synthesized particles and associated with poorly crystalline iron(III) (oxyhydr)oxides, was removed by washing the samples three times with 1.0 M HCl, followed by deionized water, each for 30 min. The final Sb/Fe molar ratio in particles was determined by dissolving the solid completely in 6.0 M HCl at 50°C in a water bath.

2.2. Characterization of Sb(V)- coprecipitated and Sb(V)- free iron (oxyhydr)oxides

Mineralogy and crystallinity of the synthesized Sb(V)- coprecipitated and Sb(V)- free iron(III) (oxyhydr)oxides were determined using micro X-ray diffraction (μ-XRD). The freeze-dried samples were mounted onto XRD sample holders and analyzed on a Bruker D8 Discover GADDS XRD2 micro-diffractometer equipped with a standard sealed tube with a Co-anode at parameters of 30 kV/30 mA. The total time measurement was 240 sec at two detector positions, 15° and 40°.

Mineralogy and solid-phase iron redox speciation were examined via ^{57}Fe Mössbauer spectroscopy. The freeze-dried sample powder was loaded into 1 cm^2 Plexiglas holders. Holders were inserted into a closed-cycle exchange gas cryostat (Janis Cryogenics, USA) under a backflow of He to minimize exposure to air. Spectra were collected at 77 K using a constant acceleration drive system (WissEL, Germany) in transmission mode with a ^{57}Co source in an Rh matrix. Analysis was carried out using the Recoil software (University of Ottawa) and the Voigt Based Fitting (VBF) routine (Lagarec and Rancourt, 1997). The Lorentzian linewidth was fixed at 0.123 mm/s during fitting, as this value was the linewidth measured on the spectrometer using a ^{57}Fe foil with an ideal thickness.

Morphologies and elemental distributions of samples were characterized using scanning electron microscopy (SEM) and transmission electron microscopy (TEM). For SEM analysis, samples were placed onto an aluminum stub using carbon adhesive tape, followed by a depositional coating of gold. The samples were then investigated using a Zeiss Crossbeam 550 L Focused Ion Beam scanning electron microscope (SEM) (Zeiss, Germany) with an acceleration voltage of 2.0 kV. For TEM analysis, samples were dispersed onto carbon-support films om copper mesh TEM grids and examined using a 200 kV field emission gun (FEG)

high-resolution analytical scanning transmission electron microscope (STEM; Thermo Fisher Spectra 300, USA).

Zeta potentials (ZP) of Sb(V)- coprecipitated samples, which represent the surface charge of samples, were determined using a Malvern Zetasizer Nano ZS (Malvern Instruments). The mineral suspension consisted of Sb(V)- coprecipitated iron (oxyhydr)oxides (5 mM), HEPES buffer (15 mM, pH = 7), and NaCl (10 mM). An aliquot of 1 mL suspension was transferred into disposable folded capillary cells and placed into the Zetasizer. Each measurement was performed in triplicate to ensure reproducibility. The zeta potential was obtained from the electrophoretic mobility by the Smoluchowski equation (Lowry et al., 2016).

2.3. Microbial Fe(III) reduction experiments

To study the effect of microbially mediated reductive dissolution and antimony mobility of Sb(V)- coprecipitated iron(III) (oxyhydr)oxides, we performed cell suspension experiments using the fermentative Fe (III)-reducer *Shewanella oneidensis* MR-1. The cells were revived from a frozen stock culture maintained in the Geomicrobiology laboratory (University of Tübingen, Germany). A pre-culture was grown under oxic conditions using Luria-Bertani (LB) liquid medium that contains 10 g/L peptone, 5 g/L yeast extract, and 10 g/L NaCl. The pre-culture was incubated for 24 h at 28°C. Following incubation, cells were harvested by centrifugation at 4300 × g for 10 min and washed twice using HEPES buffer solution to remove residual LB medium. Cell pellets were resuspended in N_2-flushed, autoclaved buffer solution, and the resulting cell suspension was quantified by measuring the optical density (OD) at 600 nm, where an OD value of 1.5 corresponded to a cell concentration of 10^9 cells/mL. The cell suspension was then added into batch reactors to achieve a final concentration of 5×10^8 cells/mL. The microbial Fe(III) reduction experiments were carried out in triplicate using serum bottles filled with 25 mL of anoxic buffer solution (HEPES 15 mM, pH 7). Sodium lactate (5 mM) and [Sb(V)- coprecipitated] iron(III) (oxyhydr) oxides (10 mM) were used as electron donors and acceptors, respectively, and AQDS (20 μM) was employed as an electron shuttle to mimic natural redox-active mediators such as natural organic matter (NOM) and extracellular polymeric substances (EPS). Serum bottles were sealed by sterilized butyl rubber stoppers and crimped with aluminum caps to maintain anoxic conditions. The bottles were incubated statically at 28°C in the dark for up to 7 days, although sampling was performed only during the first 75 h, when Fe(II) production showed measurable changes.

2.4. Determination of HCl-extracted dissolved Sb and Fe phases

During the microbial Fe(III) reduction experiments, serum bottles were transferred into a N_2-filled glovebox (MBraun Unilab Workstation, 100% N_2 atmosphere) for geochemical sampling. The suspension was periodically collected (at 3, 6, 12, 25, 35, 50, 75 h) under anoxic conditions inside the glovebox using sterile needles and syringes. An aliquot of the suspension (0.2 mL) was sampled and centrifuged to separate the aqueous and solid phases (12100 × g, 15 min). The concentration of dissolved Fe and Sb was determined from the supernatant, which was stabilized by 1 M HCl. Another aliquot of the suspension (0.2 mL) was sampled and mixed with 0.5 M HCl (30 min at 25°C in a glovebox) to extract aqueous Fe and Sb species as well as those bound to poorly crystalline iron(III) (oxyhydr)oxides. Afterwards, aqueous and solid phases were separated by centrifugation (12100 × g, 15 min) and reactive Fe and Sb were determined from the supernatant. In addition, an aliquot of the suspension (0.1 mL) was sampled and completely dissolved in 6 M HCl (8 h at 60°C in an oven inside the glovebox) to determine total Fe and Sb concentrations.

Based on the above acid extraction, the concentration of different Fe (II) fractions was quantified using the ferrozine assay (Stookey, 1970; Hegler et al., 2008). Corresponding fractions of Sb were determined by inductively coupled plasma-mass spectrometry (ICP-MS, Agilent 7900) after acidification to a final concentration of 2% HNO_3, with standard deviations < 10% for all Sb measurements.

2.5. Characterization of remaining Sb and Fe solid phases

The speciation of Fe in the remaining solid phase after reduction was examined via ^{57}Fe Mössbauer spectroscopy as described above, while the redox speciation of Sb in the solid phase was quantified using Sb K-edge X-ray absorption near-edge structure spectroscopy (XANES). Sb K-edge was recorded in fluorescence mode on diluted powders (0.2% Sb in cellulose) at cryogenic temperatures at the BioXAS beamline at Canadian Light Source (CLS) using a Si (220) monochromator. Reference standards included Sb_2O_3, $KSb(OH)_6$, tripuhyite ($SbFeO_4$; synthesized by heating equimolar amounts of Fe_2O_3 and Sb_2O_3 for 12 h at 973°C (Martinelli et al., 2002)), Sb(V) and Sb(III) adsorbed to goethite and hematite. The diluted samples and standards were pressed into pellets (7 mm diameter) and mounted on the sample holders. Data were recorded in fluorescence mode using two 32-element Ge detectors with a Zr-filter and Soller slits placed between the detector and the sample to enhance the signal-to-noise ratio. An Sb metal foil (30,491 eV) located downstream of the sample was used for energy calibration, and an Al foil was used to filter the background Fe fluorescence signal. Three replicate spectra were collected per sample. Raw Sb K-edge XANES spectra were merged and exported with the corresponding reference foil spectra. Normalization and background subtraction were performed using the ATHENA software (Ravel and Newville, 2005). The redox state of Sb was determined via linear combination fitting (LCF) of normalized Sb K-edge XANES spectra, using Sb_2O_3 (Sb(III)) and tripuhyite (Sb(V)) as reference standards. Fourier transforms of normalized Sb k^3-weighted $\chi(k)$ data were calculated over a k-range of 3 to 12.5 Å^{-1}, using a Kaiser − Bessel window function with $dk = 1$. Least-squares fittings of k^3-weighted extended X-ray absorption fine structure (EXAFS) spectra were performed using Artemis (Ravel and Newville, 2005), with theoretical phase-shift and amplitude functions calculated using the *ab initio* FEFF6 code (Ankudinov et al., 1998). Scattering paths used to model Sb K-edge EXAFS spectra were extracted from the structures of tripuhyite (Berlepsch et al., 2003). Details regarding Sb K-edge XAS analysis are provided in the SI, section S2.

3. Results

3.1. Characterization of Sb(V)- coprecipitated goethite and hematite nanoparticles

To determine the impact of Sb(V) coprecipitation on microbial reduction of iron(III) (oxyhydr)oxides as a function of particle size, we synthesized goethite and hematite with a range of different sizes in the presence of Sb(V). The identity of the synthesized phases was confirmed using μ-XRD and ^{57}Fe Mössbauer spectroscopy.

Reflections indicative of pure goethite and hematite in the presence and absence of antimony were identified in the μ-XRD patterns (Fig. 1). However, Sb(V) coprecipitation led to broadened μ-XRD reflections, which were more pronounced with decreasing sizes. Additionally, the presence of pure goethite and hematite phases was confirmed by ^{57}Fe Mössbauer spectroscopy (Fig. 2 and SI, Fig. S1, Tables S1-S2). Differences in Mössbauer fitting parameters between Sb-coprecipitated minerals and their corresponding Sb-free counterparts (SI, Tables S1-S2) revealed slight variations in magnetic properties of samples, indicating either distortion in the crystal lattice or decreases in particle sizes. Furthermore, most spectra of Sb-containing goethite and hematite exhibited two or three sextets, each corresponding to characteristic signals of goethite or hematite (Murad and Cashion, 2004; Schwertmann and Cornell, 2008). The presence of multiple sextets may be indicative of a distribution of crystallinities within samples. Notably, a collapsed phase accounted for over 20% of the area in Sb-Small Gt and Sb-Small Hm samples, which has been hypothesized to represent a mixture of

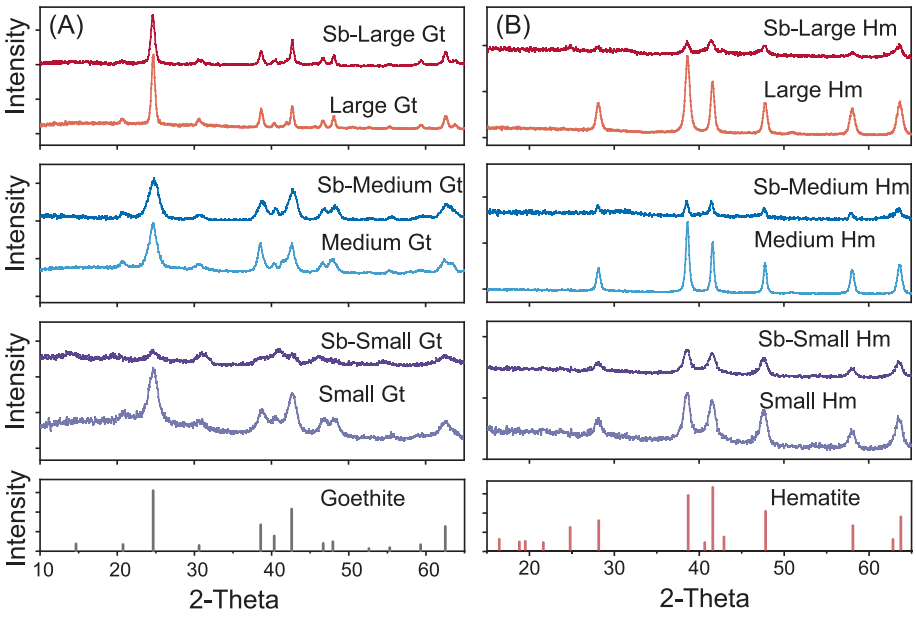

Fig. 1. XRD patterns of the synthesized goethite (A) and hematite (B) in the presence (absence) of antimony (Sb(V)) as a function of particle size. Reference patterns: standard goethite (ICDD entry 96–900-3078) and standard hematite (ICDD entry 96–900-0140). The XRD reflections broaden with decreasing particle sizes and coprecipitation with Sb(V), indicating a decrease in crystallinity.

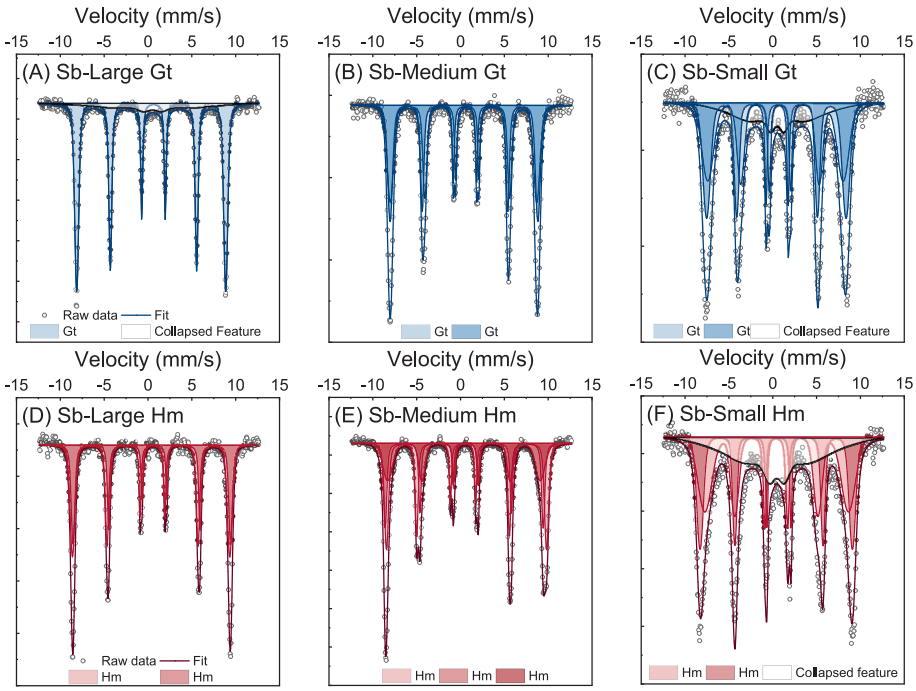

Fig. 2. Mössbauer spectra of the synthesized goethite and hematite in the presence of antimony (Sb(V)) at 77 K. Sb-Large Gt (A); Sb-Medium Gt (B); Sb-Small Gt (C); Sb-Large Hm (D); Sb-Medium Hm (E); Sb-Small Hm (F). Symbols represent experimental raw data, fit curves represent the total fit, and the shaded sextet represents the hyperfine field distribution (HFD).

poorly crystalline and/or trace element-substituted phases (Murad and Schwertmann, 1983; Latta et al., 2012). Collectively, the coprecipitation of Sb led to a lower crystallinity and distorted lattice, with relatively small changes in mineral identity.

Particle sizes were determined based on the average size of (Sb-coprecipitated) goethite and hematite particles observed in STEM and SEM images (Figs. S2-S5, Table S3). The Sb(V)-free iron(III) (oxyhydr) oxide minerals synthesized in this study were characterized as Large Gt (acicular nanoparticles with a mean length ± width of 1950 ± 360 nm), Medium Gt (acicular nanoparticles, 90 ± 10 nm), and Small Gt (acicular nanoparticles, 30 ± 10 nm); as well as Large Hm (pseudo-hexagon platelets with a mean diameter of 330 nm), Medium Hm (pseudo-hexagon platelets, 40 nm), and Small Hm (pseudo-hexagon platelets, 8 nm) (Xu et al., 2025). The corresponding Sb(V)-coprecipitated minerals exhibited notably different particle sizes: Sb-Large Gt (acicular nanoparticles, 800 ± 150 nm), Sb-Medium Gt (acicular nanoparticles, 120 ± 10 nm), and Sb-Small Gt (acicular nanoparticles, 20 ± 10 nm); and Sb-Large Hm (pseudo-hexagon platelets, 50 nm), Sb-Medium Hm (pseudo-

hexagon platelets, 30 nm), and Sb-Small Hm (pseudo-hexagon platelets, 9 nm). It is important to note that the terms "large" "medium" and "small" are relative within each mineral type, and do not imply that the Large Gt and Large Hm samples have comparable absolute particle sizes. In addition, Sb(V) coprecipitation affected particle size differently: it decreased particle size in some cases (e.g., Large Gt: from 1950 to 800 nm; Large Hm: from 330 to 50 nm; Small Gt: from 30 to 20 nm), increased particle size in others (e.g., Medium Gt: from 90 to 120 nm), and had relatively little effect in some hematite samples (e.g., Medium Hm and Small Hm). Nevertheless, the Sb-Large, Sb-Medium, and Sb-Small labels are assigned based on the corresponding Sb-free particle size produced under identical synthesis conditions to facilitate direct comparison.

3.2. Determination of Sb(V) distribution and coprecipitation extent

To determine the extent of Sb(V) coprecipitation with iron(III) (oxyhydr)oxides and its distribution, we performed HCl extraction and STEM-Energy Dispersive X-ray Spectroscopy (EDS) measurements. It is commonly assumed that the 1 M HCl-extractable fraction represents Sb (V) that is weakly adsorbed or coprecipitated with poorly crystalline iron(III) (oxyhydr)oxides, such as ferrihydrite (Vithana et al., 2018). Therefore, we first washed coprecipitated minerals with 1 M HCl and deionized water for 30 min each to remove those sorbed and poorly crystalline phases. The Sb/Fe molar ratio in highly crystalline particles was determined after complete dissolution in 6 M HCl, with the results summarized in Table 1. We prepared an initial Sb/Fe molar ratio of 1:10 for all coprecipitated systems. The highest extent of Sb(V) coprecipitation was observed for Sb-Medium Hm (8.32%), while the lowest was found in Sb-Medium Gt (2.32%). In all cases, the Sb/Fe molar ratios in the coprecipitates were lower than 10%. Overall, the extent of Sb(V) coprecipitation showed no clear correlation with particle size. However, hematite exhibited a relatively greater capacity for Sb(V) coprecipitation than goethite.

The morphology of coprecipitated particles, along with elemental distribution of Fe and Sb, is displayed in representative STEM images and corresponding EDS maps (Fig. 3). Sb-Large Gt and Sb-Medium Gt exhibited the uniform needle-like morphology typical of goethite, whereas Sb-Small Gt displayed a shorter, rod-like morphology (Fig. 3C). In the case of hematite, the typical cubic morphology was observed in Sb-Medium Hm and Sb-Small Hm. In contrast, Sb-large Hm showed a more heterogeneous morphology, featuring both typical cubic and elongated plate-like structures (Fig. 3D). In terms of chemical distribution, Fe and Sb displayed strong spatial correlation, indicating Sb coprecipitation with iron minerals. Notably, the Sb-Large Hm (Fig. 3D) displayed heterogeneous particle morphology and an uneven Sb distribution, suggesting possible structural distortion caused by the incorporation of Sb. In addition, Sb-Large Gt (Fig. 3A) and Sb-Medium Hm (Fig. 3E) displayed Sb enrichment at their particle edges, whereas other samples displayed comparatively uniform Sb distribution throughout the particles (Fig. 3B-C, D, F). Overall, Sb can coprecipitate with iron(III) minerals without altering their mineralogy and morphology, except in the case of Sb-Large Hm. Moreover, Sb was observed to be either enriched at the surface edges of mineral particles or uniformly distributed within the mineral structure.

Table 1
Elemental composition for solids precipitated from the iron (oxyhydr)oxide synthesis procedure.

Minerals	Sb/Fe molar ratio (%)	
	Synthesis solution[a]	Precipitated solids[b]
Sb-Large Gt	10	3.12 ± 0.06
Sb-Medium Gt	10	2.35 ± 0.11
Sb-Small Gt	10	4.22 ± 0.07
Sb-Large Hm	10	4.72 ± 0.09
Sb-Medium Hm	10	8.32 ± 0.44
Sb-Small Hm	10	3.86 ± 0.07

[a] Initial Sb/Fe molar ratio in the original synthesis solution.
[b] Molar % based on Sb/Fe (triplicate analysis).

3.3. Microbial reduction of Sb-coprecipitated iron(III) (oxyhydr)oxides

3.3.1. Impact of Sb coprecipitation on microbial Fe(III) reduction dynamics

To investigate the impact of Sb coprecipitation on the size-dependent reduction behavior of Sb-containing and Sb-free iron(III) (oxyhydr)oxides, we tracked the production of total Fe(II) over time ($Fe(II)_{total}$) (Fig. 4A and B). For all samples, $Fe(II)_{total}$ concentrations increased over the first 20 h, followed by a constant $Fe(II)_{total}$ concentration, indicating the cessation of microbial Fe(III) reduction. With decreasing particle sizes, the reduction extent increased for both goethite and hematite, regardless of the Sb content. $Fe(II)_{total}$ production from Sb-containing minerals was consistently lower than from their Sb-free counterparts, indicating that Sb coprecipitation with both goethite and hematite inhibited microbial Fe(III) reduction. The suppression effect was found to vary from 31 to 72% for goethite and from 24 to 80% for hematite, relative to the corresponding Sb-free samples (Fig. 4C). The strongest suppression was observed in the Sb- Large Gt (72%) and Sb-Medium Hm (80%) samples for goethite and hematite, respectively. The suppression effects were found to have no clear correlation with either Sb coprecipitation extent or particle mineralogy. However, larger particles generally exhibited more pronounced suppression.

Rate constants (k') for microbial Fe(III) reduction were derived using a pseudo-first-order kinetic model (Fig. 4), which provided a highly reliable fit to the experimental data ($R^2 > 0.99$ for all samples) (SI, Section S1.3). Rate constants increased with decreasing particle sizes for both goethite and hematite (Table S4), consistent with the observed trend in the reduction extent. In addition, the suppression of reduction kinetics in Sb-containing samples paralleled the reduction extent, with rate constant decreases ranging from 25 to 82% for goethite and from 29 to 84% for hematite. The most pronounced suppression was consistently observed in the Sb-Large Gt and Sb-Medium Hm. Collectively, these results demonstrate that Sb coprecipitation significantly influences not only the extent of microbial Fe(III) reduction but also its kinetics.

3.3.2. Impact on Sb partitioning and mobility

To investigate the partitioning behavior of Sb during microbial Fe (III) reduction, we quantified the Sb content in multiple fractions using acid extractions. In this study, the aqueous dissolved Sb was defined as the mobilized fraction, representing Sb readily released into solution. The Sb content extracted using 0.5 M HCl was considered as the reactive fraction, reflecting Sb that was either freely available or bound to poorly crystalline iron(III) (oxyhydr)oxides and thus potentially bioavailable. Sb retained within the mineral structure via coprecipitation was classified as the immobilized fraction, representing Sb that is less susceptible to mobilization under reducing environmental conditions. The total amount of Sb initially coprecipitated with iron minerals during synthesis was referred to as total solid-phase Sb.

To determine the mobility of coprecipitated Sb during microbial reduction, we quantified the dissolved Sb concentrations in the aqueous phase throughout the experiment (Fig. 5, Fig. S6). Aqueous dissolved Sb increased by varying amounts with different mineral particles during the initial 20 h but remained relatively constant thereafter. Sb-Large Gt and Sb-Medium Hm, which contained the highest Sb content in their respective mineral phases, released the greatest amounts of Sb into solution, with ~10 and ~3% of total solid-phase Sb mobilized, respectively. In contrast, the other minerals released <1.4% of total Sb, suggesting their strong retention capacity and stability as Sb sinks under anoxic conditions.

To further evaluate the mobilization potential of Sb during microbial Fe(III) reduction, the proportions of mobilized and reactive Sb fractions relative to total solid-phase Sb were evaluated as a function of the

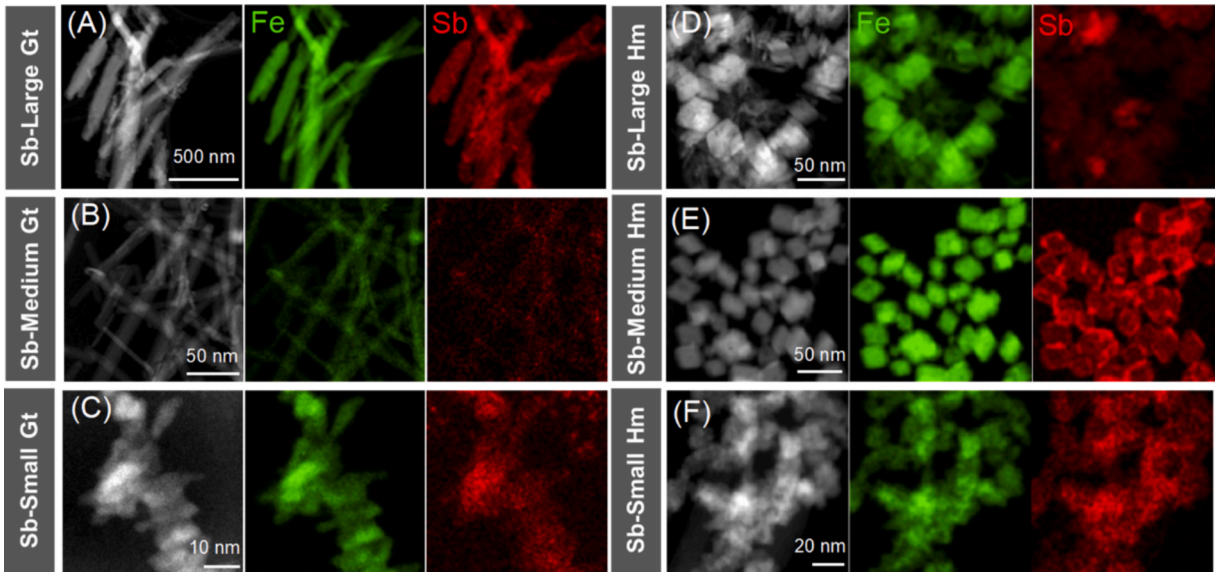

Fig. 3. Representative STEM images and corresponding EDS maps showing the morphology and Fe-Sb elemental distribution of synthesized Sb-Large Gt (A), Sb-Medium Gt (B), Sb-Small Gt (C), Sb-Large Hm (D), Sb-Medium Hm (E), and Sb-Small Hm (F) nanoparticles.

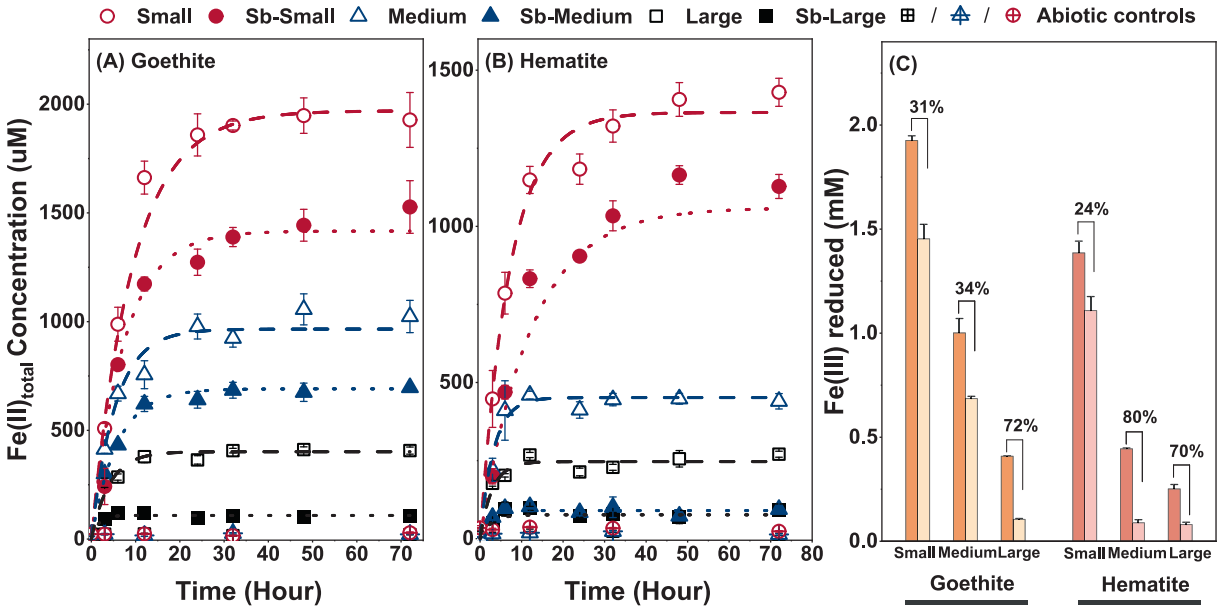

Fig. 4. Total Fe(II) production by microbial reduction of goethite (A) and hematite (B) and total reduced Fe(III) concentration after 70 h (C) as a function of particle size. The solid symbols denote Sb(V)-coprecipitated iron(III) (oxyhydr)oxides, the empty symbols represent Sb(V)-free iron(III) (oxyhydr)oxides, and the empty samples with a cross inside indicate the abiotic controls, near the zero line. The dashed or dotted lines denote the fit based on pseudo-first-order kinetics. The dark yellow and red bars denote Sb(V)-free iron(III) (oxyhydr)oxides, while the light yellow and red bars represent Sb(V)- coprecipitated iron(III) (oxyhydr)oxides. Error bars indicate standard deviations. Experimental conditions: 10 mM Fe(III) of goethite/hematite; 10^8 cells mL^{-1} *S. oneidensis* MR-1 (no cells in abiotic controls, shown as symbols without fitting lines); 20 μM AQDS; pH 7.

proportion of released Fe(II) relative to total Fe (Fig. 6). In all cases, the reactive fractions of Sb and Fe(II) were consistently higher than their mobilized fraction alone, suggesting rapid re-adsorption of released Sb and Fe(II) onto residual mineral surfaces or the formation of weakly bound Fe(II)-Sb compounds.

Two distinct Sb release patterns were observed. In the Sb-Large Gt, Sb-Large Hm and Sb-Medium Hm, reactive Sb fractions exceeded the stoichiometric dash line (1:1 release for $Sb_{fractions}/Sb_{total}$ and $Fe_{fractions}/Fe_{total}$), suggesting preferential partitioning of Sb relative to Fe into the combined aqueous and weakly bound phases. This may be related to the initially uneven distributions of Sb within the mineral structure (i.e., enriched Sb rims on Sb-Large Gt and Sb-Medium Hm) (Fig. 3A and E) or different particles with heterogeneous Sb contents (e.g., Sb-Large Hm) (Fig. 3D). These uneven variations in Sb spatial distribution would facilitate Sb release during early-stage mineral dissolution. These findings align with our previous STEM/EDS observations showing Sb enrichment at mineral surfaces and edges in Sb-Large Gt and Sb-Medium Hm (Fig. 3A, E), as well as the heterogeneous morphology and uneven Sb spatial distribution in Sb-Large Hm (Fig. 3D). Conversely, in the Sb-Medium Gt, Sb-Small Gt, and Sb-Small Hm systems, the reactive Sb fractions remained below the stoichiometric dash line, indicating preferential Sb retention by iron(III) (oxyhydr)oxide minerals during

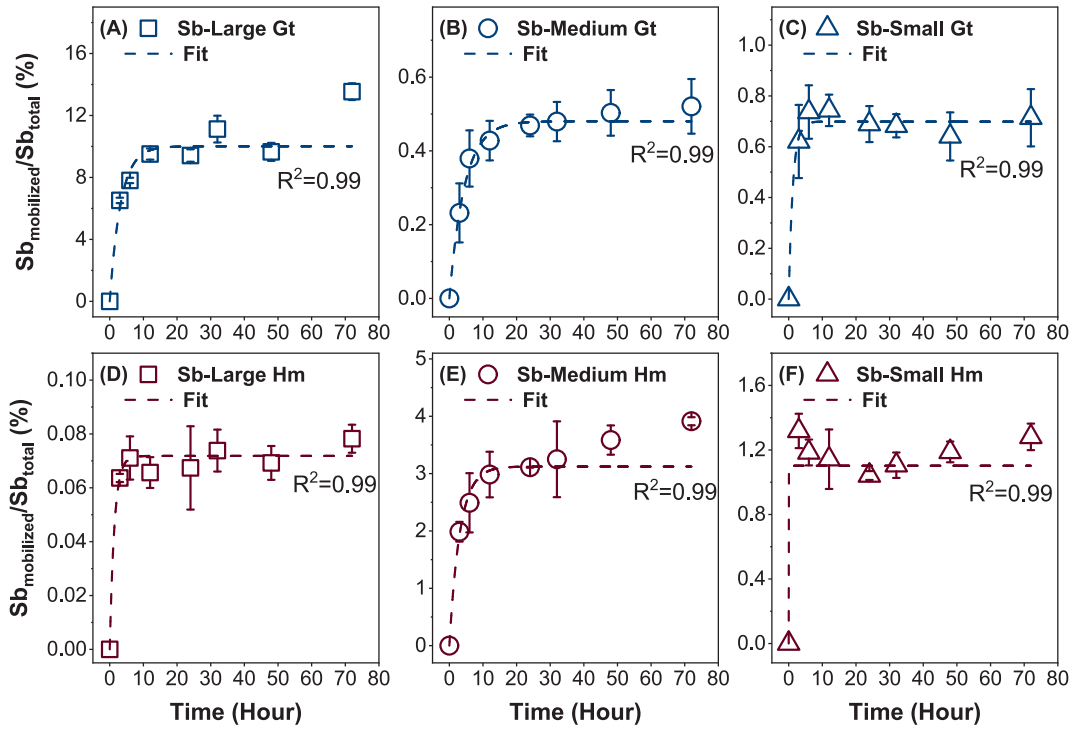

Fig. 5. Mobilized fraction of Sb (Aqueous dissolved Sb) relative to the total solid-phase Sb (initially coprecipitated Sb) of Sb-Large Gt (A), Sb-Medium Gt (B), Sb-Small Gt (C), Sb-Large Hm (D), Sb-Medium Hm (E), and Sb-Small Hm (F) nanoparticles over the course of microbial Fe(III) reduction. The symbols correspond to the average of replicates and the error bars indicate standard deviations.

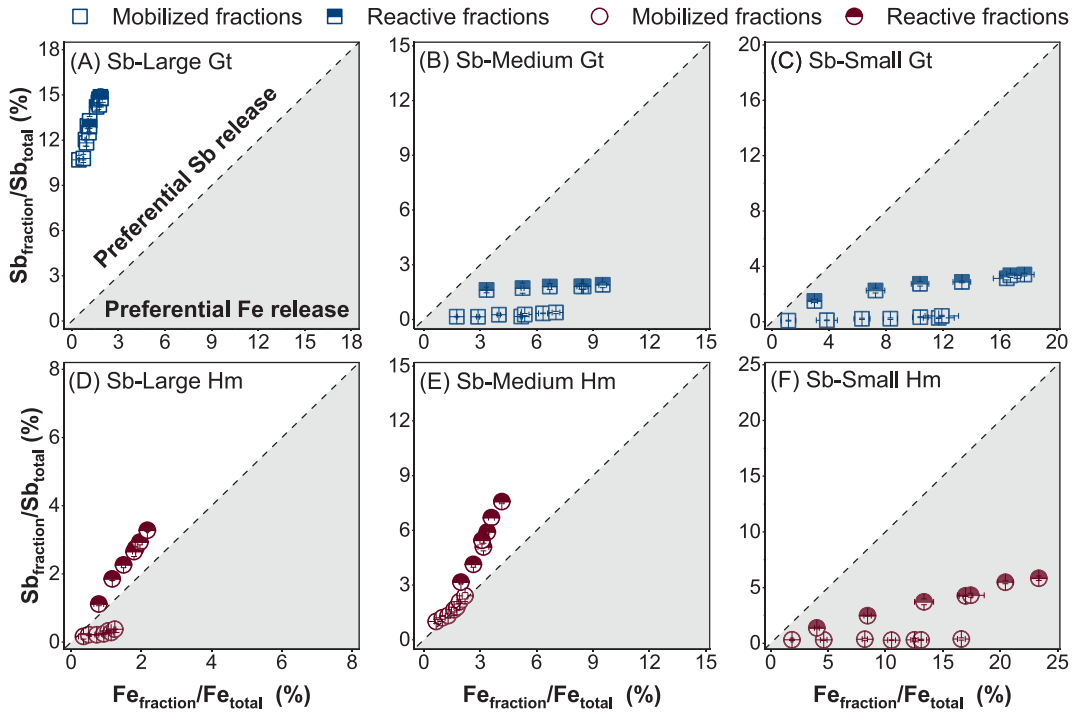

Fig. 6. Mobilized and reactive fractions of Sb relative to total Sb plotted as a function of released Fe(II) relative to total Fe for Sb-Large Gt (A), Sb-Medium Gt (B), Sb-Small Gt (C), Sb-Large Hm (D), Sb-Medium Hm (E), and Sb-Small Hm (F) nanoparticles. Empty symbols represent the mobilized fraction, while half-filled symbols represent the reactive fraction. Dashed lines denote 1:1 release for $Sb_{fractions}/Sb_{total}$ and $Fe_{fractions}/Fe_{total}$. Data following the dashed 1:1 lines indicate congruent release of the respective $Sb_{fractions}/Sb_{total}$ and $Fe_{fractions}/Fe_{total}$ during microbial Fe(III) reduction, data above the 1:1 lines labelled in white color indicate preferential Sb release in the initial phase of reductive dissolution, data below the 1:1 lines labelled in gray color indicate preferential Fe release. Symbols represent the average of replicates, with error bars denoting standard deviations.

reduction. This enhanced retention may result from either limited Sb release due to disproportionate Sb spatial distribution and intense aggregation of smaller particles, or increased Sb re-adsorption and complexation with Fe minerals due to the higher surface area of smaller-sized particles.

3.3.3. Impact on Sb speciation and local coordination environment

To determine the redox speciation of coprecipitated Sb throughout microbial Fe(III) reduction, we performed linear combination fitting (LCF) of Sb K-edge X-ray absorption spectra using Sb(V) and Sb(III) reference samples. The normalized XANES spectra of these samples closely resembled that of the pure Sb(V) reference (Fig. 7, Table S5), indicating negligible reduction of Sb(V) to Sb(III) following microbial reduction across all particle sizes.

Modelling of the Sb K-edge EXAFS spectra revealed Sb coordination by a first shell comprising 5.9–6.5 O atoms at an inter-atomic distance of 1.96–1.98 Å (Fig. 8, Table 2). This is consistent with an octahedral coordination of Sb (V) by O, thereby supporting the results of our LCF analyses of the XANES spectra (Fig. 7).

The two Sb-Fe distances were in the ranges of 3.06–3.09 Å and 3.52–3.56 Å for all Sb/Fe ratios (Table 2). The first value corresponds to the Sb-Fe distance along the edge-sharing linkage, and the second corresponds to the Sb-Fe distance along the corner-sharing link (Mitsunobu et al., 2010). The coordination numbers (CNs) of both bonds were 0.5–2.4 and 1.8–5.1, respectively, which are larger than those of Sb-Fe for the adsorbed species (Mitsunobu et al., 2010; Mitsunobu et al., 2013). The larger CNs of the Sb-Fe shells in our samples indicate that Sb (V) was incorporated into the structures of goethite or hematite. On the other hand, the CNs of the Sb-Fe shells in the samples were smaller than those of the Fe-Fe shells in pure goethite and hematite, which follow a 2 + 4 (Fe–Fe_1/Fe–Fe_2) pattern for goethite and a 3 + 4 (Fe–Fe_1/Fe–Fe_2) pattern for hematite. This may be due to (i) the increase of disorder of Fe-Fe links in the iron(III) (oxyhydr)oxide structure by Sb(V) incorporation and/or (ii) the mixing of adsorbed species present in Sb(V)-coprecipitated iron(III) (oxyhydr)oxides.

Following microbial Fe(III) reduction, the local coordination environment of Sb, including atomic distances and coordination numbers (CNs), exhibited slight variations across samples. While Sb–Fe bond distances remained consistent, CNs showed sample-dependent trends, including increases, decreases, or minimal changes. Specifically, CNs increased in the Sb-Large Gt sample after reduction, remained relatively stable in Sb-Small Gt, and decreased slightly in Sb-Medium Hm and Sb-Small Hm.

Overall, Sb K-edge EXAFS results (Fig. 8, Table 2) suggest that Sb(V) was structurally incorporated into the crystal structures of both goethite and hematite through partial hetero-valent substitution of Fe(III). However, a more detailed comparison with crystallographic models reveals the characteristic Fe backscattering environments (Figs. S7-S8). Furthermore, microbial Fe(III) reduction influenced the local coordination environment of Sb, particularly altering the coordination numbers of Sb–Fe shells, indicating a subtle redistribution of Sb within the host mineral structures.

3.3.4. Impact on mineralogy and morphology of iron(III) (oxyhydr)oxides

Mineralogy and morphology of four samples were characterized after reduction treatments. No bulk transformation of Sb-containing goethite or hematite into secondary minerals was observed in our microbial reduction treatments via Mössbauer spectroscopy (SI, Fig. S9). However, the collapsed feature area observed in Sb-Small Hm disappeared following microbial reduction (SI, Fig. S9D), suggesting that a fraction of the poorly crystalline hematite phase underwent reductive dissolution. Similarly, investigation at the nanoscale by STEM/EDS showed no obvious secondary mineralization, with no discernible changes in the morphology after microbial reduction (SI, Fig. S10). In particular, the Sb-enriched edges on Sb-Medium Hm remained clearly visible after reduction, indicating limited Sb mobilization. The remaining two samples were not analyzed, as S/TEM observations and our chemical dataset indicated no expected mineralogical differences.

To further evaluate potential changes in primary particle size, we performed a simple geometric calculation showing that a 1 nm decrease

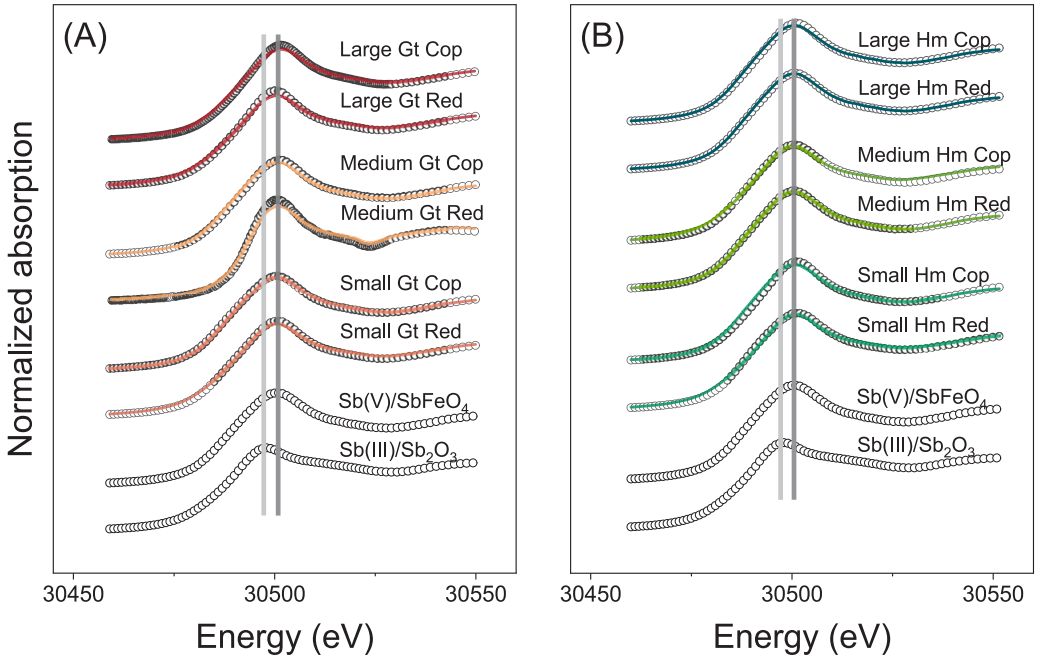

Fig. 7. Sb K-edge normalized XANES spectra for goethite (A) and hematite (B) before and after microbial Fe(III) reduction experiments. Black symbols represent experimental data, and colored lines denote the best fits. LCF indicated that Sb(III) was negligible in all samples (<2% of the LCF), with the R-factor ranging from 0.001 to 0.019. "Cop" denotes samples with Sb coprecipitated during iron(III) (oxyhydr)oxide formation. "Red" indicates the same samples following microbial Fe (III) reduction. The spectrum of medium Gt Red was collected at ESRF, while the others were collected at CLS, resulting in differences in edge jump and peak features due to beamline variations (Details in SI, S2).

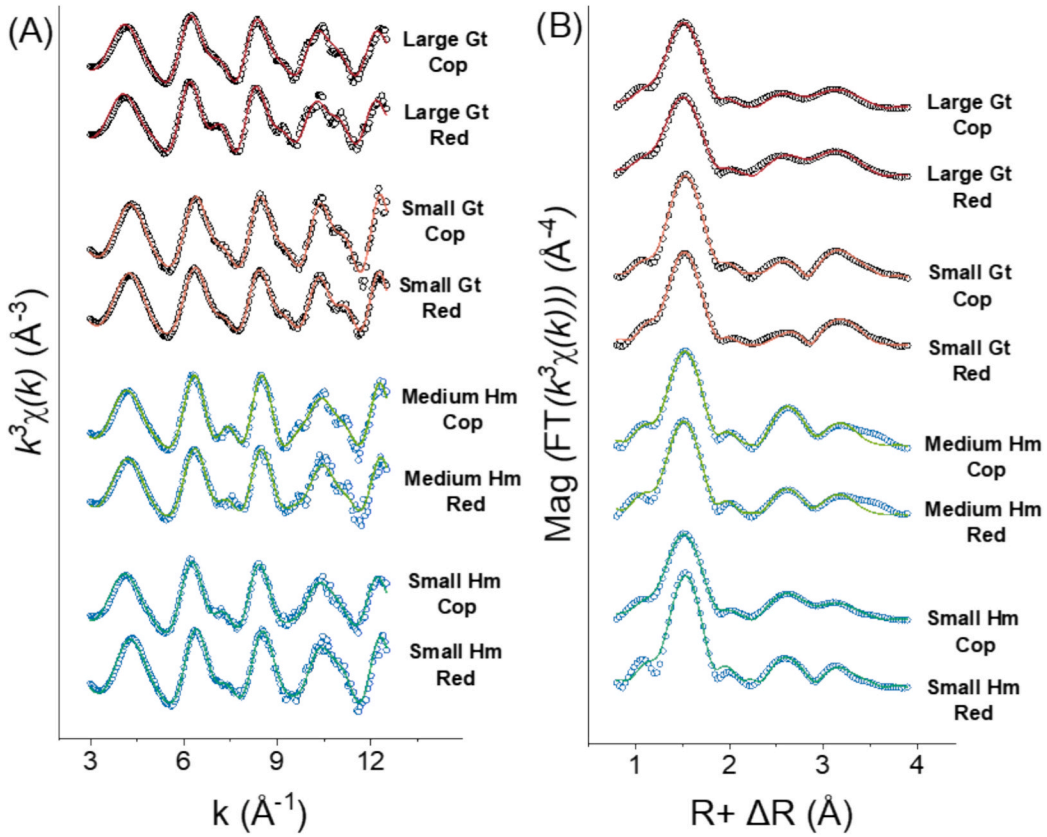

Fig. 8. Antimony K-edge k^3-weighted EXAFS spectra (A) and the corresponding Fourier Transform magnitude spectra (B) of Sb(V) coprecipitated iron(III) (oxyhydr)oxide samples collected before and after microbial Fe(III) reduction. The empty symbols and solid lines show measured data and corresponding shell fits, respectively. "Cop" denotes samples with Sb coprecipitated during iron(III) (oxyhydr)oxide formation. "Red" indicates the same samples following microbial Fe(III) reduction.

in diameter for a 10 nm spherical particle (a simple representative of the Small Hm sample) would result in ~ 27% loss of Fe (detailed calculation in Section S3, SI). Because the maximum extent of Fe(III) reduction in our experiments was < 15% for the Small Hm particles and ≤ 5% for all other systems, the amount of Fe reduced was well below the threshold needed to produce a measurable change in particle size. Collectively, these observations indicate that microbial Fe(III) reduction is expected to play only a limited role in altering mineral transformation, surface morphology, and primary particle size.

4. Discussion

4.1. Sb(V) distribution and coprecipitation behavior across iron(III) (oxyhydr)oxide mineral particle size

Antimony (Sb) has been found to coprecipitate with multiple types of iron(III) (oxyhydr)oxides, including goethite, hematite, lepidocrocite, ferrihydrite and feroxyhyte (Mitsunobu et al., 2010; Mitsunobu et al., 2013; Burton et al., 2019; Hockmann et al., 2021; Migaszewski and Gałuszka, 2025). However, the influence of particle size on Sb coprecipitation with iron(III) (oxyhydr)oxides remains poorly studied to our knowledge. Our results indicated that Sb coprecipitation occurred at Sb/Fe molar ratios below 1:10, with no clear correlation to particle size. Notably, Sb exhibited a preferential coprecipitation with hematite compared to goethite. This finding is consistent with previous observations of antimony enrichment in hematite relative to co-existing goethite in natural acid mine drainage environments, as reported by Migaszewski and Gałuszka (2025).

Given that the initial Sb-coprecipitated iron(III) (oxyhydr)oxides were washed with 1 M HCl, it is assumed that weakly bound Sb and poorly crystalline iron(III) (oxyhydr)oxides were effectively removed. Consequently, the Sb fraction subsequently extracted with 6 M HCl is attributed to Sb associated with highly crystalline precipitated complexes, strongly adsorbed phases, or structurally incorporated within the mineral matrix. Although no distinct Sb-precipitated phases were identified in our μ-XRD measurements (Fig. 1), the potential existence of such complexes in limited amounts cannot be entirely ruled out. They may exist as an amorphous phase, constitute less than 5% of the total mineral content, and/or exhibit peak overlap with the synthesized iron (III) (oxyhydr)oxides, making them difficult to distinguish by μ-XRD analysis alone.

Antimony(V) is usually coordinated octahedrally with six oxygen atoms. Its ionic radius is 0.60 Å, comparable to that of 0.65 Å for Fe(III) (Mitsunobu et al., 2010). The similarity of ionic radius could facilitate the substitution of Sb(V) for Fe(III) within the iron(III) (oxyhydr)oxide lattice, which was supported by previous studies (Mitsunobu et al., 2010; Mitsunobu et al., 2013; Burton et al., 2019; Karimian et al., 2019) and our EXAFS data (Fig. 8, Table 2). Heterovalent substitution generally requires charge compensation, potentially through the loss of protons, as illustrated by the reaction:

$$\equiv Fe(III) + 2H^+ = \equiv Sb(V)$$

The loss of some of the H atoms may not be critical for preserving the goethite structure; such loss may instead lead to the collapse of tunnels between its double chains (Bolanz et al., 2013). In contrast, the coupling of Fe(III)-Sb(V) with H loss appears to be limited or excluded in hematite samples. Accommodating a greater amount of Sb(V) within a hematite-related structure likely requires cation disordering to prevent face-sharing between FeO_6 octahedra (Bolanz et al., 2013). These structural modifications result in decreased crystallinity, as evidenced by the poorly crystalline features and the presence of collapsed regions in the μ-XRD patterns (Fig. 1) and Mössbauer spectra (Fig. 2) following Sb

Table 2
Antimony K-edge EXAFS shell-fit results for the Sb-containing iron (oxyhydr) oxides, before and after microbial Fe(III) reduction, as a function of particle size. CN, R, ΔE_0 and σ^2 denote the coordination number, inter-atomic distance, energy shift and Debye-Waller factor, respectively.[a]

Sample	Path	CN (−)[b]	R (Å)	ΔE_0[c](eV)	σ^2 (Å^2)[d]	R-factor[e]
Large Gt Cop	Sb-O	6.4 ± 0.6	1.97 ± 0.02	3.9 ± 1.2	0.003 ± 0.001	0.010
	Sb-Fe_1	1.5 ± 0.6	3.09 ± 0.03		0.005 ± 0.002	
	Sb-Fe_2	3.6 ± 1.3	3.56 ± 0.05		0.005 ± 0.002	
Large Gt Red	Sb-O	6.5 ± 0.7	1.97 ± 0.02	2.5 ± 1.5	0.003 ± 0.001	0.013
	Sb-Fe_1	2.2 ± 0.7	3.09 ± 0.03		0.006 ± 0.002	
	Sb-Fe_2	5.1 ± 1.6	3.56 ± 0.05		0.006 ± 0.002	
Small Gt Cop	Sb-O	5.9 ± 0.5	1.96 ± 0.03	8.8 ± 1.2	0.001 ± 0.001	0.009
	Sb-Fe_1	0.6 ± 0.3	3.06 ± 0.00		0.002 ± 0.001	
	Sb-Fe_2	2.0 ± 0.7	3.54 ± 0.06		0.002 ± 0.001	
Small Gt Red	Sb-O	6.4 ± 0.5	1.96 ± 0.02	8.1 ± 0.8	0.003 ± 0.000	0.007
	Sb-Fe_1	0.5 ± 0.2	3.06 ± 0.00		0.003 ± 0.001	
	Sb-Fe_2	1.8 ± 0.4	3.54 ± 0.07		0.003 ± 0.001	
Medium Hm Cop	Sb-O	6.3 ± 0.5	1.97 ± 0.02	6.3 ± 1.0	0.002 ± 0.001	0.007
	Sb-Fe_1	2.2 ± 0.5	3.06 ± 0.01		0.002 ± 0.001	
	Sb-Fe_2	2.4 ± 0.5	3.52 ± 0.09		0.002 ± 0.001	
Medium Hm Red	Sb-O	6.1 ± 0.6	1.97 ± 0.02	6.2 ± 1.5	0.002 ± 0.001	0.016
	Sb-Fe_1	1.3 ± 0.5	3.06 ± 0.00		0.003 ± 0.002	
	Sb-Fe_2	1.9 ± 0.8	3.52 ± 0.09		0.003 ± 0.002	
Small Hm Cop	Sb-O	6.5 ± 0.5	1.98 ± 0.02	4.3 ± 1.0	0.003 ± 0.001	0.006
	Sb-Fe_1	2.4 ± 1.0	3.08 ± 0.02		0.005 ± 0.002	
	Sb-Fe_2	2.8 ± 0.9	3.56 ± 0.05		0.005 ± 0.002	
Small Hm Red	Sb-O	6.1 ± 0.7	1.97 ± 0.03	9.1 ± 1.5	0.002 ± 0.000	0.023
	Sb-Fe_1	1.5 ± 0.6	3.06 ± 0.00		0.002 ± 0.002	
	Sb-Fe_2	1.9 ± 0.9	3.53 ± 0.08		0.002 ± 0.002	

[a] Fit uncertainties are given for the last significant figure.
[b] The amplitude reduction factor was set to 0.9 (Yan et al., 2022a), and the uncertainty associated with this estimate has been included in the error of CN.
[c] The energy shift was constrained to a single value for all shells for each spectrum.
[d] For each spectrum, one fitted value for the Debye-Waller factor was allowed for near-neighbour oxygens, and another one for metal(loid) scatterers.
[e] R-factor = $\Sigma_i(data_i\text{-}fit_i)^2/\Sigma_i\ data_i$.

incorporation.

The observed variations in Sb(V) coprecipitation with goethite and hematite are strongly governed by the synthesis conditions (Table S7, Fig. S11). First, pH plays a dominant role because Sb(V) exists primarily as the negatively charged $Sb(OH)_6^-$ species across pH 4–12 (Filella et al., 2002a). For Large and Medium goethite, the rapid increase to pH > 12 during synthesis generates strongly negative surface charges on the initial ferrihydrite/goethite precursors (pH_{pzc} ~ 7–9.5) (Xu et al., 2025), leading to strong electrostatic repulsion and, consequently, limited Sb adsorption and incorporation. In contrast, Large and Medium hematite were synthesized at acidic pH (<3), where precursor surfaces are positively charged and electrostatically favorable for $Sb(OH)_6^-$ uptake, resulting in substantially higher Sb coprecipitation.

Second, Fe(III) concentration influences supersaturation and nucleation kinetics. Small goethite (250 mM Fe) and Medium hematite (200 mM Fe) were synthesized at the highest degrees of supersaturation, promoting rapid nucleation and the formation of numerous small nuclei with abundant reactive sites. This environment enhances Sb-Fe co-complexation and occlusion, yielding relatively high Sb coprecipitation. In contrast, Large goethite (50 mM Fe) and Large hematite (20 mM Fe) formed under lower supersaturation, producing fewer but larger, better-ordered crystals that incorporated less Sb(V).

Third, Sb-Fe complexation during early hydrolysis contributes significantly to Sb retention. The formation of outer- or inner-sphere Sb–Fe complexes is favored at lower pH, lower temperature, and higher nucleation density conditions (Sun et al., 2023), consistent with the highest Sb incorporation observed in Small Gt and Medium Hm.

Finally, reaction time affects the degree to which initially adsorbed Sb(V) is structurally incorporated during recrystallization (Burton et al., 2020). Longer aging periods (e.g., 50 days for Small Gt; 7–10 days for hematite syntheses) allow more extensive dissolution-reprecipitation and atomic rearrangement, facilitating the solid-state diffusion of adsorbed Sb into the crystal lattice. In contrast, shorter reaction times (e.g., 24 h for Medium Gt; <2h for Small Hm) limit this process, resulting in more modest or minimal Sb incorporation.

Together, these factors, pH-dependent surface charge, Fe supersaturation, Sb-Fe complexation kinetics, and reaction time provide a basis for the distinct Sb coprecipitation extents observed across different particle sizes and synthesis conditions (Table S7, Fig. S11).

4.2. Inhibition of microbial Fe(III) reduction by Sb-containing minerals

The microbial and chemical reduction of iron(III) (oxyhydr)oxide is one of the most important biogeochemical processes on Earth that significantly impacts the fate and mobility of nutrients, trace elements, and pollutants (Borch et al., 2010; Kappler et al., 2021). Previous studies have demonstrated that microbial Fe(III) mineral reduction was influenced by multiple factors, such as mineral phase, crystallinity, particle size, and trace element substitution (Yan et al., 2008; Bose et al., 2009; Cutting et al., 2009; Echigo et al., 2012). However, to our knowledge, the present work is the first to investigate Fe(III) reduction kinetics and Sb behavior as a function of particle size under microbially mediated reducing conditions. Microbial reduction of Sb-containing goethite and hematite in our study was inhibited to varying degrees. For goethite, the extent of reduction decreased by 31–72%, and the reduction rate constant by 24–82% when Sb was present. In the case of Sb-containing hematite, the extent of reduction was decreased by 24–80%, and the rate constant by 29–62% compared to Sb-free hematite (Table S4, Fig. 4).

It was expected that Sb(V) coprecipitation, like other element substitution, would alter the physicochemical properties of the iron(III) (oxyhydr)oxides, and consequently affect the kinetics and extent of microbial Fe(III) reduction. Here, we considered five factors that could have caused the inhibition effects: (1) enhanced stabilization by Sb replacement of Fe in the crystal structure, (2) decrease in surface area, (3) more negative surface charge that affect the interaction of the electron shuttle AQDS with the Fe(III) mineral surfaces (4) occupation of reactive surface sites by re-absorbed Fe(II) and Sb(V) ions (5) Sb(V) serving as a competing electron acceptor, and (6) potential toxicity of Sb species toward microbial cells.

As we discussed above, Sb(V) can structurally substitute for Fe(III) in the coprecipitated iron(III) (oxyhydr)oxides, which was supported by previous studies (Mitsunobu et al., 2010; Mitsunobu et al., 2013; Burton et al., 2019; Karimian et al., 2019) and our EXAFS data (Fig. 8, Table 2). In addition, it has been widely reported that Sb(V) coprecipitation and sorption can act to stabilize ferrihydrite and the poorly-crystalline Fe

(III) oxyhydroxysulfate mineral schwertmannite against proton-promoted dissolution (Rastegari et al., 2022; Moghaddam et al., 2024). The stabilizing effect reflected the greater binding strength of SbO_6-FeO_6 edge and double-corner sharing linkage in Sb(V)- coprecipitated iron(III) minerals compared with the corresponding FeO_6-FeO_6 linkage in Sb-free iron minerals. Although reductive dissolution differs from proton-driven dissolution, the enhanced stability of the SbO_6-FeO_6 linkage may contribute to the observed suppression of reduction.

Surface area has been identified as a key controlling factor for both biotic and abiotic Fe(III) reduction in several studies (Roden and Zachara, 1996; Roden, 2003). The observed decrease in reduction kinetics and extent may be attributed to the decline in accessible surface area due to Sb(V) coprecipitation. In goethite, Sb coprecipitation led to a notable decrease in surface area (ranging from 4 to 51%) (Table 3), likely due to changes in mineral crystallinity and aggregation pattern. Although the decline in surface area (4–51%) did not fully correlate with the extent of reduction inhibition (31–72%) in Sb-containing goethite (SI, Fig. S12), it likely played a substantial role in the overall suppression effect. In hematite, Sb coprecipitation led to a substantial increase in surface area by 33 and 44% for Large Hm and Medium Hm, respectively, while a decrease by 20% was observed for Small Hm. The increase in surface area is likely a consequence of multiple factors, including changes in particle size, morphology, defects and crystallinity. The previous results of μ-XRD patterns, ^{57}Fe Mössbauer spectra, and TEM images collectively indicate that Sb-containing Large Hm and Medium Hm exhibited decreased crystallinity and smaller particle size, with the exclusive development of secondary morphologies in the Large Hm samples (Fig. 3D).

To further quantify the extent to which surface area changes contributed to the observed suppression in Fe(III) reduction, we normalized the reduction rate constant (k') by specific surface area (SSA) to isolate other intrinsic reactivity effects (e.g., surface charge). This is due to the Sb coating around the minerals, which also influences their surface charge (Fig. S13), as discussed in detail in the following section. We defined an index:

$$I = \frac{(k'/SSA)_{Sb}}{(k'/SSA)_{noSb}}$$

An $I = 1$ indicates that differences in Fe(III) reduction rate between Sb-coprecipitated and Sb-free minerals are primarily attributable to surface-area changes associated with Sb coprecipitation. Values of $I \neq 1$ indicate that other factors discussed in this section could play an important role.

Table 3
Reduction rate constants of goethite and hematite normalized by BET-derived surface area.

Minerals	Rate constant h^{-1} ($\times 10^{-3}$)	BET SA m^2/g	Minerals	Rate constant h^{-1} ($\times 10^{-3}$)	BET SA m^2/g	I [a]
Large Gt	0.90 ± 0.03	18.2 ± 1.3	Sb-Large Gt	0.16 ± 0.02	8.9 ± 1.3	0.36
Medium Gt	2.55 ± 0.24	125.8 ± 7.1	Sb-Medium Gt	1.80 ± 0.07	121.1 ± 1.4	0.73
Small Gt	6.13 ± 0.09	200.8 ± 9.1	Sb-Small Gt	4.60 ± 0.61	145.3 ± 7.1	1.04
Large Hm	0.43 ± 0.05	44.1 ± 0.1	Sb-Large Hm	0.17 ± 0.06	58.5 ± 1.3	0.29
Medium Hm	1.00 ± 0.06	54.6 ± 3.0	Sb-Medium Hm	0.17 ± 0.12	78.5 ± 7.6	0.12
Small Hm	5.13 ± 0.16	134.8 ± 6.9	Sb-Small Hm	3.64 ± 0.53	108.1 ± 5.8	0.89

[a] $I = (k'/SSA)_{Sb}/(k'/SSA)_{no\ Sb}$. $I = 1$ indicates that the observed reduction rate difference results primarily from indirect changes in surface area or particle size caused by Sb co-precipitation. $I \neq 1$ indicates that other factors, rather than surface area alone, control observed differences in reduction behavior.

As shown in Table 3, the I values for Sb-Small Gt, Sb-Small Hm, and Sb-Medium Gt are close to 1, suggesting that their reduction behavior is largely governed by surface area changes induced by Sb coprecipitation. In contrast, the I values for Sb-Large Gt, Sb-Large Hm, and Sb-Medium Hm deviate substantially from 1, indicating that other differences, rather than surface area alone, control their reduction behavior. Collectively, these results show that Sb-induced changes in surface area primarily explain the suppression of Fe(III) reduction in the Small Gt, Small Hm, and Medium Gt samples, but only partially in the Large Gt, Large Hm, and Medium Hm samples.

The potentially inhibitory adsorption of AQDS on Sb-coprecipitated iron(III) (oxyhydr)oxides may also contribute to the observed differences in reduction. Negatively charged AQDS was employed as an electron shuttle between Fe(III)-reducing bacteria and minerals in our systems, to mimic natural redox-active mediators such as NOM and EPS (Lovley et al., 1996; Bai et al., 2020). The zeta potential measurements under experimental conditions, as shown in SI, Fig. S13, indicate that Sb (V) coprecipitation either produces no significant changes (Medium and Small Gt, Small Hm) or decreases the surface charge of iron(III) (oxyhydr)oxides (Large Gt and Large and Medium Hm). Specifically, Sb-free iron(III) (oxyhydr)oxides exhibit a positive surface charge of ~ 30 mV, whereas Sb-Large Gt and Sb-Medium Hm show a reversal to −30 mV, while Sb-Small Hm decreases slightly to 25 mV. Therefore, this potential inhibitory effect is pronounced for Large Gt and Medium Hm, where the surface charge shifts from positive to negative, most likely due to the Sb-enriched edges observed in STEM images (Fig. 3A, E). It has been extensively shown that negatively charged organic molecules adsorb on iron(III) (oxyhydr)oxide via electrostatic interactions (Parikh and Chorover, 2006; Fang et al., 2012). Thus, Sb-coprecipitated minerals, which exhibit less positively charged surfaces than their pure mineral counterparts at pH 7.0, may provide lower electrostatic attraction to AQDS. Consequently, this could inhibit the Fe(III) reduction of Sb coprecipitated minerals. Notably, the two negatively charged Sb-coprecipitated minerals exhibited the greatest degree of reduction suppression among minerals of the same type.

Occupation of reactive surface site by re-adsorbed Fe(II) and Sb(V) may play a role in inhibiting microbial Fe(III) reduction. It has been reported that Fe(II) bound to surfaces of Fe(III) minerals may block reactive surface sites, thereby inhibiting their further reduction (Liu et al., 2001; Roden and Urrutia, 2002; Xu et al., 2025). In our experiments, both released Fe(II) and Sb(V) were found to re-adsorb onto mineral surface, as indicated by the consistently higher reactive fractions (sorbed + aqueous species) of Fe(II) and Sb(V) relative to their mobilized (aqueous) fractions (Fig. 6). This interpretation was further supported by the decrease in the average CNs of Sb-Fe paths observed in Sb-Small Hm and Gt samples, suggesting that a fraction of the structurally incorporated Sb(V) was transformed into a weakly bound, adsorbed form (Fig. 8, Table 2). Moreover, the re-adsorbed Fe(II) and Sb (V) likely form surface complexes that further occupy reactive sites on the mineral surface, a process consistent with previous studies showing that divalent metal ions can form ternary complexes with Sb(V) on iron mineral surface (Fan et al., 2016; Kumar et al., 2025). Collectively, these results indicate that re-adsorbed Fe(II) and Sb(V) likely block reactive mineral surface sites accessible to AQDS and thereby contribute to the observed inhibition of microbial Fe(III) reduction.

In addition to the physicochemical alterations in Sb-containing iron (III) (oxyhydr)oxides, the coprecipitated Sb(V) may serve as a competing electron acceptor with Fe(III), potentially contributing to the observed variations in microbial Fe(III) reduction behavior. Several studies have reported that Sb(V) can undergo reduction to Sb(III) on the surface of magnetite, green-rust, mackinawite and nontronite, which are common Fe(II)-bearing phases in subsurface environments (Kirsch et al., 2008; Mitsunobu et al., 2008; Ilgen et al., 2012; Zhang et al., 2022). However,

our Sb K-edge XANES data clearly show that Sb remained exclusively in the pentavalent state throughout all experiments (Fig. 7), allowing us to rule out Sb(V) reduction as a competing electron-accepting pathway in our systems. The absence of Sb(V) reduction can be attributed to (i) the lack of known metabolic pathways and reductase in *S. oneidensis* MR-1 for direct enzymatic Sb(V) reduction, (ii) the absence of magnetite and green rust, minerals known to reduce Sb(V), as transformation products in our experiments (Mitsunobu et al., 2008; Zhang et al., 2022), and (iii) the limited ability of biogenic, surface-bound Fe(II) on goethite and hematite to transfer electrons to Sb(V) at circumneutral pH (Burton et al., 2020).

The final potential inhibiting factor in our experiments may be attributed to Sb toxicity. Previous studies have reported that Sb can decrease metabolic activity in the environment (An and Kim, 2009; Wang et al., 2021; Moreno-Andrade et al., 2023). Notably, Moreno-Andrade et al. (2023) demonstrated that the concentrations causing a 50% decrease in bacterial luminescence (IC_{50}), relative to the Sb-free control, were 57.3 and 104.2 mg/L for Sb(V) and 11.2 and 12.2 mg/L for Sb(III) in methanogenic and fermentative microbial communities under anaerobic conditions, respectively. In our experiments, the role of Sb toxicity is therefore considered minor for two reasons. First, Sb(III) was not detected in any treatment, eliminating the most toxic species. Second, aqueous Sb(V) concentrations remained low, with values lower than ~ 5 mg/L in all mineral systems (Fig. S10), which were well below the previously reported inhibitory thresholds for Sb(V) (Moreno-Andrade et al., 2023).

Collectively, to explain the observed inhibitory impacts on microbial Fe(III) reduction, we propose six potential hypotheses: (1) enhanced structural stabilization; (2) decreased surface area (primarily affecting the Small Gt, Small Hm, and Medium Gt samples); (3) increased negative surface charge (most pronounced for Large Gt and Medium Hm); (4) occupation of reactive surface sites by re-adsorbed Fe(II) and Sb(V) ions; (5) Sb(V) acting as a competing electron acceptor; and (6) potential toxicity of Sb species to microbial cells. Based on our experimental observations, we conclude that the first four assumptions are the dominant contributors to the observed inhibition, whereas electron acceptor competition and microbial toxicity likely play only minor roles under the conditions investigated.

The suppression effect of trace elements on microbial Fe(III) reduction has been reported by previous work on goethite and ferrihydrite. Specifically, Bousserrhine et al. (1999) found that aluminum (Al) and chromium (Cr) substitution in goethite dramatically decreased their bacterial reduction. This inhibition was attributed to the accumulation of Al and Cr on the goethite surface, which likely impeded bacterial access to reactive sites. Zegeye et al. (2021) reported that the rate of ferrihydrite reduction decreased by approximately 50% in the presence of Sb(V) loadings, while the overall extent of reduction was only slightly inhibited (~10%) compared to bio-reduction of pure ferrihydrite. However, no previous work has specifically determined the effect of Sb coprecipitation on microbial Fe(III) reduction of nanoscale goethite and hematite. Building on previous findings and our current observations, it is evident that the suppression of microbial Fe(III) reduction is influenced not only by the type of trace element incorporated into the structure, but also by the specific mineral phase and particle size.

4.3. Retention and mobility of Sb during microbial Fe(III) reduction

We conducted microbial reduction experiments of Sb(V)-coprecipitated iron(III) (oxyhydr)oxides to assess the partitioning of Sb under reducing conditions. Concurrent with reductive dissolution, coprecipitated Sb was released into both aqueous and surface-bound Sb fractions. We observed incongruent release behavior between Sb and Fe fractions: i) reactive fractions of Sb were released at a higher rate relative to corresponding fractions of Fe, or ii) reactive fractions of Sb were released at a lower rate relative to corresponding fractions of Fe (Fig. 6). These observed behaviors occurred without correlation to the mineral particle sizes, mineral types and Sb coprecipitation contents.

Several potential processes may be responsible for driving the observed redistribution of Sb in mobilized and reactive Sb fractions. First, the presence of reactive Fe(II) or Fe(III)-reducing microorganisms may trigger the reduction of Sb(V) to Sb(III), which has a greater tendency to adsorb onto iron(III) (oxyhydr)oxides than Sb(V) (Leuz et al., 2006). However, the Sb K-edge XANES data indicate this assumption was of negligible importance, since Sb(V) persisted across all experimental treatments for all samples (Fig. 7).

Second, Sb(V) initially coprecipitated with iron(III) (oxyhydr)oxides exhibited a heterogeneous distribution within the mineral matrix in some cases, which may control the subsequent partitioning behavior. Most Sb(V) is likely structurally substituted for Fe(III) within the mineral structure due to their similar ionic size and bond distances in Sb-O (1.97–2.00 Å) and Fe-O (1.98–2.00 Å) octahedra. This structural incorporation was supported by previous studies (Mitsunobu et al., 2010; Mitsunobu et al., 2013) as well as our EXAFS data (Fig. 8, Table 2). Intriguingly, Sb exhibited enrichment at the edges of Sb-Large Gt and Sb-Medium Hm and displayed a disproportionate distribution in Sb-Large Hm (Fig. 3). This heterogeneity correlated with relatively high mobilized Sb concentration (Fig. 5) and an enhanced Sb release relative to corresponding Fe (Fig. 6). The localized enrichment of Sb at mineral edges suggests that a portion of Sb(V) may be weakly associated rather than structurally substituted within the iron(III) (oxyhydr)oxide matrix. As a result, these loosely bound Sb species are more susceptible to mobilization during reductive dissolution, leading to an enhanced Sb release compared to Fe. This is further confirmed by the increase in the average CNs of Sb–Fe paths observed in the Sb-Large Gt sample after microbial reduction, indicating the release of a fraction of weakly bound Sb(V) into solution, while the remaining Sb(V) was predominantly incorporated or strongly retained within the mineral structure (Fig. 8, Table 2). Furthermore, these minerals exhibit comparatively lower surface areas, fewer reactive sites and negative surface charges, limiting Sb(V) re-adsorption onto the remaining mineral surfaces. These combined effects of high Sb release and low Sb adsorption likely contribute to the overall increased Sb mobilization observed in the system.

In contrast, Sb displayed comparatively homogenous distribution in Sb-Medium Gt, Sb-Small Gt and Sb-Small Hm (Fig. 3), despite exhibiting decreased Sb release relative to corresponding Fe (Fig. 6). This incongruent release behavior of Sb may be attributed to multiple factors: (i) Mobilized Sb existed predominantly as negatively charged species $Sb(OH)_6^-$ in experimental suspensions at circumneutral pH, which may outcompete mobilized Fe^{2+} for adsorption sites on the remaining positively charged mineral surfaces (SI, Fig. S13); (ii) The presence of mobilized Fe^{2+} may promote the sorption capacity of Sb(V) through electrostatic interactions and the formation of amorphous precipitates or inner-sphere surface complexes (Yan et al., 2022b). This was supported by the decrease in the average CNs of Sb-Fe paths observed in Sb-Small Hm, suggesting that a fraction of the structurally incorporated Sb (V) was transformed into a weakly bound, adsorbed form (Fig. 8, Table 2). The mechanisms were also supported by previous studies showing that aqueous Fe(II) can enhance Sb(V) sorption onto soils and goethite (Fan et al., 2016).

4.4. Environmental Implications

This study investigated the effect of Sb(V) on the microbial Fe(III) reduction of nanosized goethite and hematite and the resulting Sb repartitioning under controlled laboratory conditions, which contributes to a broader understanding of Sb(V) behavior in natural mining-impacted soils. Antimony is widely reported to be closely associated with natural iron(III) (oxyhydr)oxides, which have been identified in various Sb-contaminated sites, including the Ichinokawa Sb mine, Japan (Mitsunobu et al., 2010), the Beaver Brook antimony deposit, Canada (Radková et al., 2020), the Xikuangshan mining area (Zhou et al., 2024), and the Macleay River catchment, Australia (Johnston et al., 2020a).

Seasonal fluctuations in the water table driven by rainfall or irrigation can establish alternating oxic-anoxic conditions. Under reducing conditions, Sb(V) that is sorbed to or structurally incorporated within iron (III) (oxyhydr)oxides may affect microbial Fe(III) reduction, thereby affecting the environmental mobility and geochemical fate of Sb(V).

Our findings demonstrate that the structural incorporation of Sb significantly inhibited both the extent and kinetics of microbial Fe(III) reduction in goethite and hematite, with a decrease ranging from 25 to 80%. Hence, the reductive susceptibility of iron(III) (oxyhydr)oxides is markedly influenced by the presence of trace element substitutions. In short, Sb incorporation increases the stability of goethite and hematite by a factor of 1.3 to 4.5, with a more pronounced effect observed in larger particles. Here, we define the "stabilization factor" as the ratio of the Fe(III) reduction extent in the unmodified (pure) mineral to that in the Sb-substituted counterpart. This stabilization factor quantifies the decrease in mineral bioavailability as electron acceptor resulting from Sb incorporation and is a more straightforward term that can be used as guidelines for environmental management. It also has significant implications for accurately modeling redox processes in natural environments, especially in systems subject to fluctuating redox conditions such as mining-impacted soils.

In addition, our results indicated that under microbially mediated reducing conditions, a maximum of approximately 10% of structurally incorporated Sb(V) was released from iron(III) (oxyhydr)oxide matrices. A portion of this mobilized Sb was likely re-adsorbed onto the mineral surfaces, further limiting its mobility. These combined findings suggest that structural incorporation of Sb within goethite or hematite may serve as an effective and stable sink for Sb in the environment, even under redox-dynamic conditions. When extrapolating our results to longer time periods, we caution that our work focused on the short term and aimed to investigate if and how Sb is mobilized during periods of anoxia. Hence, Sb mobility and speciation may evolve differently over extended periods in natural systems. Long-term laboratory and field studies have shown that multiple oxic-anoxic cycling in paddy soils and mining-impacted environments can substantially alter Sb behavior, including enhanced mobilization during oxic phases and partial Sb(V) reduction or sulfide-associated sequestration under prolonged anoxic conditions (Ye et al., 2020; He et al., 2024). Seasonal temperature oscillations have also been shown to influence redox metabolism and the mobility of As and Sb (Johnston et al., 2020b). Although investigating these long-term and environmentally fluctuating conditions is beyond the scope of the present work, future studies can build on the insights gained here and incorporate extended redox cycling and field relevant conditions to ascertain Sb stability across a broader range of geochemical settings.

5. Conclusions

This study investigated the microbially mediated Fe(III) reduction behavior of Sb-containing iron(III) (oxyhydr)oxide minerals, focusing on the influence of particle size and the resulting mobility and fate of Sb. Our findings revealed that:

- **Sb incorporation:** Sb can be structurally incorporated into nanoscale goethite and hematite particles of different sizes at molar percentages of up to 8%, though the extent of coprecipitation displayed no clear correlation with mineral type or particle size.
- **Inhibition of Fe(III) reduction:** The presence of Sb inhibited both the extent and kinetics of microbial Fe(III) reduction across all samples with varying particle sizes, with suppression ranging from 25 to 80%.
- **Low and incongruent Sb release:** Sb release under reducing conditions remained low (<10% of total Sb for goethite and < 4% of total Sb for hematite) and did not correspond to reductive release of Fe, indicating incongruent release behavior.

These findings suggest that Sb incorporation into goethite and hematite can act as an effective sink for Sb immobilization, while also enhancing the stability of iron(III) (oxyhydr)oxides under microbially reducing conditions.

Data availability

All data displayed in the figures is available from Mendeley Data https://doi.org/10.17632/h3732b29pp.2.

CRediT authorship contribution statement

Xiyang Xu: Writing – review & editing, Writing – original draft, Visualization, Methodology, Investigation, Funding acquisition, Formal analysis, Conceptualization. **Prachi Joshi:** Writing – review & editing, Writing – original draft, Supervision, Project administration, Methodology, Funding acquisition, Conceptualization. **Kerstin Hockmann:** Writing – review & editing, Methodology, Funding acquisition. **Carolin L. Dreher:** Writing – review & editing, Methodology, Data curation. **Valerie A. Schoepfer:** Writing – review & editing, Methodology, Funding acquisition, Data curation. **Po-Yen Tung:** Writing – review & editing, Methodology, Funding acquisition. **John C. Walmsley:** Writing – review & editing, Supervision, Project administration, Methodology, Funding acquisition. **Andreas Kappler:** Writing – review & editing, Supervision, Project administration, Methodology, Funding acquisition. **Muammar Mansor:** Writing – review & editing, Writing – original draft, Supervision, Project administration, Methodology, Funding acquisition, Conceptualization.

Declaration of competing interest

The authors declare that they have no known competing financial interests or personal relationships that could have appeared to influence the work reported in this paper.

Acknowledgement

We thank Franziska Schaedler and Lars Grimm for their technical support in the lab; Liane G. Benning and Vladimir V. Roddatis for their initial TEM characterization of the nanoscale iron(III) (oxyhydr)oxides; Tsz Ho Chiu for BET surface area measurements; and Martina Bottaro for ICP-MS analysis. MM acknowledges the support by the DFG, project ID 494840258. This research was supported by the CSC scholarship (202106010075). This project has received funding from the European Union's Horizon 2020 research and innovation programme under grant agreement No. 101005611 for EXCITE Transnational Access conducted at Wolfson Electron Microscope Suite, University of Cambridge, Department of Materials Science and Metallurgy and we acknowledge use of the Thermo Fisher Spectra 300 STEM funded by EPSRC under grant EP/R008779/1. Antimony XAS measurements were conducted at the Canadian Light Source (CLS) synchrotron, (grant No. 39G13933) and at the European Synchrotron Radiation Facility (ESRF) (grant No. EV-584). The authors gratefully acknowledge the Tübingen Structural Microscopy Core Facility (funded by the Federal Ministry of Education and Research (BMBF) and the Baden-Württemberg Ministry of Science as part of the Excellence Strategy of the German Federal and State Governments) for their support with SEM analysis. We acknowledge support from the Open Access Publishing Fund of the University of Tübingen.

Appendix A. Supplementary material

Details about synthesis and characterization of nanoparticulate goethite; Sb K-edge XANES and EXAFS measurements and data analysis; characterization of Sb-containing goethite and hematite after microbial Fe(III) reduction (PDF). Supplementary material to this article can be

found online at https://doi.org/10.1016/j.gca.2026.01.034.

References

An, Y.-J., Kim, M., 2009. Effect of antimony on the microbial growth and the activities of soil enzymes. Chemosphere 74, 654–659.

Ankudinov, A.L., Ravel, B., Rehr, J., Conradson, S., 1998. Real-space multiple-scattering calculation and interpretation of x-ray-absorption near-edge structure. Phys. Rev. B 58, 7565.

Bai, Y., Mellage, A., Cirpka, O.A., Sun, T., Angenent, L.T., Haderlein, S.B., Kappler, A., 2020. AQDS and redox-active NOM enables microbial Fe (III)-mineral reduction at cm-scales. Environ. Sci. Technol. 54, 4131–4139.

Berlepsch, P., Armbruster, T., Brugger, J., Criddle, A., Graeser, S., 2003. Tripuhyite, FeSbO4, revisited. Mineral. Mag. 67, 31–46.

Bolanz, R.M., Bläss, U., Ackermann, S., Ciobotă, V., Rösch, P., Tarcea, N., Popp, J., Majzlan, J., 2013. The effect of antimonate, arsenate, and phosphate on the transformation of ferrihydrite to goethite, hematite, feroxyhyte, and tripuhyite. Clay Clay Min. 61, 11–25.

Borch, T., Kretzschmar, R., Kappler, A., Cappellen, P.V., Ginder-Vogel, M., Voegelin, A., Campbell, K., 2010. Biogeochemical redox processes and their impact on contaminant dynamics. Environ. Sci. Technol. 44, 15–23.

Bose, S., Hochella Jr, M.F., Gorby, Y.A., Kennedy, D.W., McCready, D.E., Madden, A.S., Lower, B.H., 2009. Bioreduction of hematite nanoparticles by the dissimilatory iron reducing bacterium Shewanella oneidensis MR-1. Geochim. Cosmochim. Acta 73, 962–976.

Bousserrhine, N., Gasser, U., Jeanroy, E., Berthelin, J., 1999. Bacterial and chemical reductive dissolution of Mn-, Co-, Cr-, and Al-substituted goethites. Geomicrobiol J. 16, 245–258.

Burton, E.D., Hockmann, K., Karimian, N., 2020. Antimony Sorption to Goethite: effect of Fe (II)-Catalyzed Recrystallization. ACS Earth Space Chem. 4, 476–487.

Burton, E.D., Hockmann, K., Karimian, N., Johnston, S.G., 2019. Antimony mobility in reducing environments: the effect of microbial iron (III)-reduction and associated secondary mineralization. Geochim. Cosmochim. Acta 245, 278–289.

Cooper, R.G., Harrison, A.P., 2009. The exposure to and health effects of antimony. Indian J. Occup. Environ. Med. 13, 3–10.

Cutting, R., Coker, V., Fellowes, J., Lloyd, J., Vaughan, D., 2009. Mineralogical and morphological constraints on the reduction of Fe (III) minerals by Geobacter sulfurreducens. Geochim. Cosmochim. Acta 73, 4004–4022.

Echigo, T., Aruguete, D.M., Murayama, M., Hochella Jr, M.F., 2012. Influence of size, morphology, surface structure, and aggregation state on reductive dissolution of hematite nanoparticles with ascorbic acid. Geochim. Cosmochim. Acta 90, 149–162.

Fan, J.-X., Wang, Y.-J., Fan, T.-T., Dang, F., Zhou, D.-M., 2016. Effect of aqueous Fe (II) on Sb (V) sorption on soil and goethite. Chemosphere 147, 44–51.

Fang, L., Cao, Y., Huang, Q., Walker, S.L., Cai, P., 2012. Reactions between bacterial exopolymers and goethite: a combined macroscopic and spectroscopic investigation. Water Res. 46, 5613–5620.

Filella, M., Belzile, N., Chen, Y.-W., 2002a. Antimony in the environment: a review focused on natural waters: I. Occurrence. Earth-Sci. Rev. 57, 125–176.

Filella, M., Belzile, N., Chen, Y.-W., 2002b. Antimony in the environment: a review focused on natural waters: II. Relevant solution chemistry. Earth-Sci. Rev. 59, 265–285.

Filella, M., Hennebert, P., Okkenhaug, G., Turner, A., 2020. Occurrence and fate of antimony in plastics. J. Hazard. Mater. 390, 121764.

Filella, M., Williams, P.A., Belzile, N., 2009. Antimony in the environment: knowns and unknowns. Environ. Chem. 6, 95–105.

Fu, X., Xie, X., Charlet, L., He, J., 2023. A review on distribution, biogeochemistry of antimony in water and its environmental risk. J. Hydrol. 625, 130043.

Guo, X., Wu, Z., He, M., Meng, X., Jin, X., Qiu, N., Zhang, J., 2014. Adsorption of antimony onto iron oxyhydroxides: adsorption behavior and surface structure. J. Hazard. Mater. 276, 339–345.

He, M., Wang, N., Long, X., Zhang, C., Ma, C., Zhong, Q., Wang, A., Wang, Y., Pervaiz, A., Shan, J., 2019. Antimony speciation in the environment: recent advances in understanding the biogeochemical processes and ecological effects. J. Environ. Sci. 75, 14–39.

He, Y., Yang, Y., Chi, W., Hu, S., Chen, G., Wang, Q., Cheng, K., Guo, C., Liu, T., Xia, B., 2024. Biogeochemical cycling in paddy soils controls antimony transformation: Roles of iron (oxyhydr) oxides, organic matter and sulfate. J. Hazard. Mater. 464, 132979.

Hegler, F., Posth, N.R., Jiang, J., Kappler, A., 2008. Physiology of phototrophic iron (II)-oxidizing bacteria: implications for modern and ancient environments. FEMS Microbiol. Ecol. 66, 250–260.

Herath, I., Vithanage, M., Bundschuh, J., 2017. Antimony as a global dilemma: Geochemistry, mobility, fate and transport. Environ. Pollut. 223, 545–559.

Hochella Jr, M.F., Lower, S.K., Maurice, P.A., Penn, R.L., Sahai, N., Sparks, D.L., Twining, B.S., 2008. Nanominerals, mineral nanoparticles, and earth systems. Science 319, 1631–1635.

Hockmann, K., Karimian, N., Schlagenhauff, S., Planer-Friedrich, B., Burton, E.D., 2021. Impact of antimony (V) on iron (II)-catalyzed ferrihydrite transformation pathways: a novel mineral switch for feroxyhyte formation. Environ. Sci. Technol. 55, 4954–4963.

Ilgen, A.G., Foster, A.L., Trainor, T.P., 2012. Role of structural Fe in nontronite NAu-1 and dissolved Fe (II) in redox transformations of arsenic and antimony. Geochim. Cosmochim. Acta 94, 128–145.

Jang, Y.S., Zhang, Y., Boyanov, M.I., O'Loughlin, E.J., Stetten, L., Kemner, K.M., Kwon, M.J., 2025. Phosphate-modulated transformation of Sb (V)-bearing ferrihydrite under microbial iron-and sulfate-reducing conditions. Geochim. Cosmochim. Acta.

Johnston, S.G., Bennett, W.W., Doriean, N., Hockmann, K., Karimian, N., Burton, E.D., 2020a. Antimony and arsenic speciation, redox-cycling and contrasting mobility in a mining-impacted river system. Sci. Total Environ. 710, 136354.

Johnston, S.G., Karimian, N., Burton, E.D., 2020b. Seasonal temperature oscillations drive contrasting arsenic and antimony mobilization in a mining-impacted river system. Water Resour. Res. 56, e2020WR028196.

Journet, E., Balkanski, Y., Harrison, S.P., 2014. A new data set of soil mineralogy for dust-cycle modeling. Atmos. Chem. Phys. 14, 3801–3816.

Kappler, A., Bryce, C., Mansor, M., Lueder, U., Byrne, J.M., Swanner, E.D., 2021. An evolving view on biogeochemical cycling of iron. Nat. Rev. Microbiol. 19, 360–374.

Karimian, N., Burton, E.D., Johnston, S.G., 2019. Antimony speciation and mobility during Fe (II)-induced transformation of humic acid-antimony (V)-iron (III) coprecipitates. Environ. Pollut. 254, 113112.

Kirsch, R., Scheinost, A., Rossberg, A., Banerjee, D., Charlet, L., 2008. Reduction of antimony by nano-particulate magnetite and mackinawite. Mineral. Mag. 72, 185–189.

Kumar, R., Jing, C., Yan, L., 2025. A critical review on arsenic and antimony adsorption and transformation on mineral facets. J. Environ. Sci. 153, 56–75.

Lagarec, K., Rancourt, D., 1997. Extended Voigt-based analytic lineshape method for determining N-dimensional correlated hyperfine parameter distributions in Mössbauer spectroscopy. Nucl. Instrum. Methods Phys. Res., Sect. B 129, 266–280.

Latta, D.E., Bachman, J.E., Scherer, M.M., 2012. Fe electron transfer and atom exchange in goethite: Influence of Al-substitution and anion sorption. Environ. Sci. Technol. 46, 10614–10623.

Leuz, A.-K., Mönch, H., Johnson, C.A., 2006. Sorption of Sb (III) and Sb (V) to goethite: influence on Sb (III) oxidation and mobilization. Environ. Sci. Technol. 40, 7277–7282.

Liu, C., Zachara, J.M., Gorby, Y.A., Szecsody, J.E., Brown, C.F., 2001. Microbial reduction of Fe (III) and sorption/precipitation of Fe (II) on Shewanella putrefaciens strain CN32. Environ. Sci. Technol. 35, 1385–1393.

Liu, J., Pearce, C.I., Shi, L., Wang, Z., Shi, Z., Arenholz, E., Rosso, K.M., 2016. Particle size effect and the mechanism of hematite reduction by the outer membrane cytochrome OmcA of Shewanella oneidensis MR-1. Geochim. Cosmochim. Acta 193, 160–175.

Lovley, D.R., Coates, J.D., Blunt-Harris, E.L., Phillips, E.J., Woodward, J.C., 1996. Humic substances as electron acceptors for microbial respiration. Nature 382, 445–448.

Lowry, G.V., Hill, R.J., Harper, S., Rawle, A.F., Hendren, C.O., Klaessig, F., Nobbmann, U., Sayre, P., Rumble, J., 2016. Guidance to improve the scientific value of zeta-potential measurements in nanoEHS. Environ. Sci. Nano 3, 953–965.

Mansor, M., Xu, J., 2020. Benefits at the nanoscale: a review of nanoparticle-enabled processes favouring microbial growth and functionality. Environ. Microbiol. 22, 3633–3649.

Martinelli, A., Ferretti, M., Buscaglia, V., Cabella, R., Lucchetti, G., 2002. Formation and decomposition of the rutile-type compound FeSbO 4. J. Therm. Anal. Calorim. 70, 123–127.

Migaszewski, Z.M., Gałuszka, A., 2025. Primary Fe-(hydr) oxides and pyrite as carriers of arsenic and antimony: an overlooked problem in acid mine drainage areas. Sci. Total Environ. 977, 179400.

Mitsunobu, S., Muramatsu, C., Watanabe, K., Sakata, M., 2013. Behavior of antimony (V) during the transformation of ferrihydrite and its environmental implications. Environ. Sci. Technol. 47, 9660–9667.

Mitsunobu, S., Takahashi, Y., Sakai, Y., 2008. Abiotic reduction of antimony (V) by green rust (Fe4 (II) Fe2 (III)(OH) 12SO4· 3H2O). Chemosphere 70, 942–947.

Mitsunobu, S., Takahashi, Y., Terada, Y., Sakata, M., 2010. Antimony (V) incorporation into synthetic ferrihydrite, goethite, and natural iron oxyhydroxides. Environ. Sci. Technol. 44, 3712–3718.

Moghaddam, M.H., Karimian, N., Johnston, S.G., Choppala, G., Rastegari, M., Burton, E. D., 2024. Antimony (V) sorption and coprecipitation with ferrihydrite: an examination of retention mechanisms and the selectivity of commonly-applied extraction procedures. J. Hazard. Mater. 480, 136297.

Moreno-Andrade, I., Sierra-Alvarez, R., Pérez-Rangel, M., Barrera, C., Field, J.A., Pat-Espadas, A., 2023. Antimony toxicity upon microorganisms from aerobic and anaerobic environments. J. Environ. Sci. Health A 58, 61–68.

Murad, E., Cashion, J., 2004. Mössbauer Spectroscopy of Environmental Materials and Their Industrial Utilization. Kluwer Academic Publishers Group, Dordrecht, The Netherlands.

Murad, E., Schwertmann, U., 1983. The influence of aluminium substitution and crystallinity on the Mössbauer spectra of goethite. Clay Min. 18, 301–312.

Parikh, S.J., Chorover, J., 2006. ATR-FTIR spectroscopy reveals bond formation during bacterial adhesion to iron oxide. Langmuir 22, 8492–8500.

Qiu, C., Majs, F., Douglas, T.A., Schmidt, M., Trainor, T.P., 2018. In situ structural study of Sb (V) adsorption on hematite (1102) using X-ray surface scattering. Environ. Sci. Technol. 52, 11161–11168.

Radková, A.B., Jamieson, H.E., Campbell, K.M., 2020. Antimony mobility during the early stages of stibnite weathering in tailings at the Beaver Brook Sb deposit, Newfoundland. Appl. Geochem. 115, 104528.

Rastegari, M., Karimian, N., Johnston, S.G., Doherty, S.J., Hamilton, J.L., Choppala, G., Hosseinpour Moghaddam, M., Burton, E.D., 2022. Antimony (V) incorporation into schwertmannite: critical insights on antimony retention in acidic environments. Environ. Sci. Technol. 56, 17776–17784.

Ravel, B., Newville, M., 2005. ATHENA, ARTEMIS, HEPHAESTUS: data analysis for X-ray absorption spectroscopy using IFEFFIT. J. Synchrot. Radiat. 12, 537–541.

Roden, E.E., 2003. Fe (III) oxide reactivity toward biological versus chemical reduction. Environ. Sci. Technol. 37, 1319–1324.

Roden, E.E., Urrutia, M.M., 2002. Influence of biogenic Fe (II) on bacterial crystalline Fe (III) oxide reduction. Geomicrobiol J. 19, 209–251.
Roden, E.E., Zachara, J.M., 1996. Microbial reduction of crystalline iron (III) oxides: influence of oxide surface area and potential for cell growth. Environ. Sci. Technol. 30, 1618–1628.
Schwertmann, U., Cornell, R.M., 2008. Iron Oxides in the Laboratory: Preparation And Characterization. John Wiley & Sons.
Stookey, L.L., 1970. Ferrozine-–a new spectrophotometric reagent for iron. Anal. Chem. 42, 779–781.
Sun, Q., Liu, C., Fan, T., Cheng, H., Cui, P., Gu, X., Chen, L., Ata-Ul-Karim, S.T., Zhou, D., Wang, Y., 2023. A molecular level understanding of antimony immobilization mechanism on goethite by the combination of X-ray absorption spectroscopy and density functional theory calculations. Sci. Total Environ. 865, 161294.
Vithana, C.L., Johnston, S.G., Dawson, N., 2018. Divergent repartitioning of copper, antimony and phosphorus following thermal transformation of schwertmannite and ferrihydrite. Chem. Geol. 483, 530–543.
Wang, A., He, M., Ouyang, W., Lin, C., Liu, X., 2021. Effects of antimony (III/V) on microbial activities and bacterial community structure in soil. Sci. Total Environ. 789, 148073.
Wang, W., He, M., Lin, C., Ouyang, W., Liu, X., 2024. Unveiling the Influence of Antimony Substitution on the Surface Properties and Adsorption Behavior of Ferrihydrite: from Molecular Mechanisms to Environmental Implications. Environ. Sci. Technol. 58, 14475–14485.
Wilson, S.C., Lockwood, P.V., Ashley, P.M., Tighe, M., 2010. The chemistry and behaviour of antimony in the soil environment with comparisons to arsenic: a critical review. Environ. Pollut. 158, 1169–1181.
Xie, J., Coker, V.S., O'Driscoll, B., Cai, R., Haigh, S.J., Lloyd, J.R., 2023. Microbial reduction of antimony (V)-bearing ferrihydrite by Geobacter sulfurreducens. Appl. Environ. Microbiol. 89 e02175-02122.
Xu, X., Mansor, M., Li, G., Chiu, T.H., Haderlein, S.B., Kappler, A., Joshi, P., 2025. Size-dependent reduction kinetics of iron oxides in single and mixed mineral systems. Environ. Sci. Technol. 59, 2519–2530.
Yan, B., Wrenn, B.A., Basak, S., Biswas, P., Giammar, D.E., 2008. Microbial reduction of Fe (III) in hematite nanoparticles by Geobacter sulfurreducens. Environ. Sci. Technol. 42, 6526–6531.
Yan, L., Chan, T., Jing, C., 2022a. Mechanistic study for antimony adsorption and precipitation on hematite facets. Environ. Sci. Technol. 56, 3138–3146.
Yan, Y., Wan, B., Mansor, M., Wang, X., Zhang, Q., Kappler, A., Feng, X., 2022b. Co-sorption of metal ions and inorganic anions/organic ligands on environmental minerals: a review. Sci. Total Environ. 803, 149918.
Ye, L., Meng, X., Jing, C., 2020. Influence of sulfur on the mobility of arsenic and antimony during oxic-anoxic cycles: differences and competition. Geochim. Cosmochim. Acta 288, 51–67.
Zegeye, A., Carteret, C., Mallet, M., Billet, D., Ferté, T., Chang, C.S., Hauet, T., Abdelmoula, M., 2021. Effect of Sb on precipitation of biogenic minerals during the reduction of Sb-bearing ferrihydrites. Geochim. Cosmochim. Acta 309, 96–111.
Zhang, Y., O'Loughlin, E.J., Kwon, M.J., 2022. Antimony redox processes in the environment: a critical review of associated oxidants and reductants. J. Hazard. Mater. 431, 128607.
Zhou, J., Tian, H., Zhu, C., Hao, J., Gao, J., Wang, Y., Xue, Y., Hua, S., Wang, K., 2015. Future trends of global atmospheric antimony emissions from anthropogenic activities until 2050. Atmos. Environ. 120, 385–392.
Zhou, W., Liu, P., Ye, Z., Wen, B., Beckie, R.D., Zhou, A., Zhou, Z., Zhou, J., 2024. Antimony mobility in soil near historical waste rock at the world's largest Sb mine, Central China. Sci. Total Environ. 921, 171194.